BMBF Verbundprojekt

Reports on DKRZ Resources 2022

PalMod – Paleo Modelling Initiative Phase II:

From the Last Interglacial to the Anthropocene –
Modelling a Complete Glacial Cycle

Principal Investigators: Mojib Latif[1],
Tatiana Ilyina[2],
Michael Schulz[3]

(1) GEOMAR, Kiel (to whom correspondence should be sent)
(2) MPI-M, Hamburg
(3) MARUM, Bremen

Executive Summary

The report summarizes the individual reports of the projects associated to the consortium project **PalMod Phase II** and covers the time period from 2022-01-01 to 2022-10-31 unless stated otherwise.

Table of Contents

Summary

The good news for the year 2022 was, that the workflow interruptions due to COVID19 were reduced in 2022, as compared to 2021.
The bad news for the year 2022 was, that there where multiple difficulties for the PalMod consortium to use Mistral and the new HLRE4 system Levante as expected in Q1 and Q2.

Overall, usage of the supercomputer during the last 12 months was severely hampered because of the following difficulties:

- at the end of 2021, Mistral was unavailable for ~2 months for production simulations as large experiments from other projects occupied the machine. This impacted PalMod experiments by reducing model turnover from the usual 700 years/day to less than 50 years/day which led to a significant delay of the planned experiments.
- This was followed in 2022 by a difficult transition from Mistral (HLRE3) to Levante (HLRE4).
    - First, Mistral was plagued by an increasing number of node failures towards the end of its lifetime.
    - Secondly, the new system Levante was delayed by several months.
    - In addition, once Levante became available, problems with compilers and changing environments resulted in much longer porting times of the individual and combined model components than were initially anticipated.

The reasons for this are mutually dependent.
On Levante the models were not ready to run which meant that more time and effort had to be invested into the porting of the models, in turn leading to fewer simulations being run on Mistral.
This meant that first production simulations could only be resumed by the end of June with even longer delays for the fully coupled models that include interactive ice sheet and solid earth components. In all, all WGs were strongly handicapped until at least the middle of 2022 or 3rd quarter of 2022 and the numerous difficulties led to the expiration of requested compute resources on the new and old system.

Block Grant for PalMod Consortia	Granted	Used resources in Q1 (from ¼ granted)	Used resources in Q2 (from ¼ granted)	Used resources in Q3 (from ¼ granted)
Levante CPU nodes [n*h]	1.251.706	0 %	8 %	WG1 65% WG2. 75% WG 69% CC 12%

1. Project 989 / WG1

Project title: PalMod WG1 - The Physical System
Project leader: G. Lohmann (AWI), U. Mikolajewicz (MPI-M)
Sublead: G.Lohmann (AWI), V.Klemann (GFZ), U.Mikolajewicz (MPI-M), M.Prange (MARUM), (MPI-M), R.Winkelmann (PIK), T.Martin (GEOMAR)
Allocation period: 01.01.2022 – 30.09.2022

1.1 Report on resources used in 2022

At **MPI-Met**, we performed an ensemble of 9 transient simulations with our fully coupled MPI-ESM-CR-mPISM-VILMA model system. The simulations were initiated at 26,000 years BP and run to present-day, following a 20,000 yearlong asynchronous spin-up. The individual members of the ensemble differ in their model tuning and in their initial conditions. The model simulations all capture the main climate events during the last deglaciation. The major deglaciation of the northern hemispheric ice sheets occurs in all simulations between 16,000 - 9,000 years BP, which is in good agreement with ice-sheet reconstructions. However, present-day ice-sheet volumes in the Northern Hemisphere are slightly overestimated in the model. All simulations simulate abrupt ice-sheet instabilities known as Heinrich events (Figure 1). During these events, the addition of freshwater through discharge of ice and melting of icebergs leads to a weakening of the AMOC that is accompanied by a cooling over the North Atlantic. The timing and strength of the simulated Heinrich events however varies between simulations, indicating that these events are part of the internal variability of the model. Therefore, it is unlikely that the timing of the modelled events will coincide with the timing of the observed/reconstructed events.
In a suite of simulations with the coupled ice sheet-solid earth model mPISM-VILMA, we investigated the sensitivity of Heinrich events characteristics to a variety of boundary forcing perturbations. Our simulations show that surface mass balance has the largest effect on surge cycle length, with ice- surface temperature and geothermal heatflux also affecting the cycle length, but to a lesser degree. Ocean and sea-level forcing as well as different frequencies of the same forcing have a negligible effect on the surge cycle length. The simulations also highlight that only a certain parameter range exists under which ice-sheet oscillations can be maintained. Transitioning from an oscillatory state to a persistent ice streaming state can result in an ice volume loss of up to 26% for the respective ice stream drainage basin under otherwise constant climate conditions. We show that the Mackenzie ice stream is susceptible to undergoing such a transition in response to all tested positive climate perturbations.
We also performed our first asynchronously coupled simulations of MIS3 with the MPI-ESM-CR-mPISM-VILMA model system. The simulations started from 65,000 BP and extended through the Last Glacial Maximum to 10,000 years BP. Both simulations show the characteristic quasi-periodic Heinrich events during the MIS3 period. The AMOC strength remains stable throughout the MIS3 period and only weakens during the simulated Heinrich events. Sea-surface temperatures show a similar pattern during MIS3, but start to increase

during the deglaciation. The magnitude of the warming is, however, most likely underestimated because of the asynchronous coupling.
Over the last months, the running of production simulations was severely hampered by the transition from the Mistral system to the new Levante HPC. Problems with compilers and changing environments at the start of Levante resulted in much longer porting times of the individual and combined model components than we had anticipated. A consequence of this delay was the expiration of compute resources on the new and old system. The reasons for this are mutually dependent. On Levante the models were not ready to run which meant that we had to invest more time and effort into the porting of the models, hence, fewer simulations could be run on Mistral. We have now a working version of the fully coupled model on Levante and are currently optimizing its performance. Therefore, we are confident that we can resume production runs very soon, so that allocated resources will be used up in the coming months.

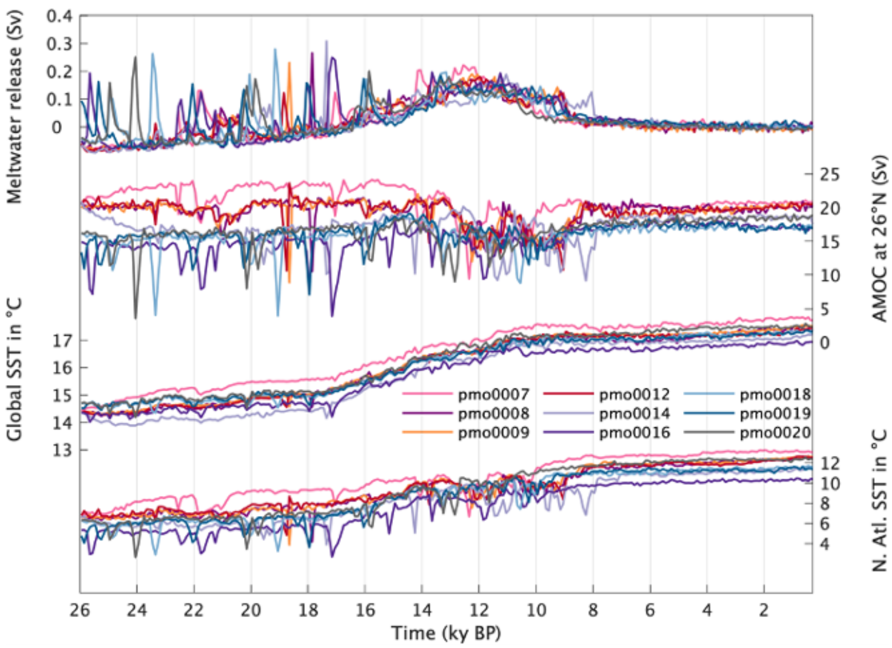

Figure 1: *Fully-coupled simulations of the last deglaciation. We show (from top to bottom) meltwater release, AMOC strength at 1,000 m depth at 26°N, and global and north Atlantic sea surface temperatures for each ensemble member.*

The **GFZ** (WP1.4-TP1) utilized the VIscoelastic Lithosphere and MAntle model VILMA to reconstruct relative sea-level changes and solid earth deformation in PalMod. In 2022, Hereon provided computing time for the GFZ. We did not use all requested computing time as there had been difficulties to compile and run VILMA on the new system Levante.
In order to analyze the GIA response for improved Earth structures, we applied the 3D Earth structure ensemble consisting of 18 members (Bagge et al., 2021), which is derived from seismic tomography as geodynamic constraints and considers deviations in the conversion from temperatures to viscosity (Fig. 2).

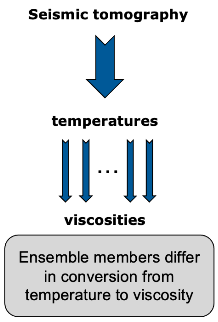

Figure 2: *Scheme for the calculation of the Earth structure ensemble from seismic tomography to viscosity following Steinberger (2016), Steinberger and Calderwood (2006) and Bagge et al. (2021).*

We worked on the refinement of the 3D Earth structure and combined the ensemble of global structures (Bagge et al., 2020) with a 3D regional Antarctic lithosphere structure (Haeger et al., 2022). For the combination, we mapped the regional Antarctic lithosphere structure into the global VILMA domain. We implemented a smooth transition from temperature structure in the global model to a constant temperature of 1300°C at the lithospheric base of the Antarctic model. A 7°-wide band around the Antarctic core region was constructed to transition from the Antarctic temperature structure to that of the global model. For the conversion from the new combined temperature structure to a viscosity structure, we chose parameters from one existing ensemble member with activation enthalpy factor 0.4 and radial viscosity profile s16. Figure 3 shows the difference for the viscosity of the old and the refined Earth structure and for the predicted uplift rates for the VILMA model output for the configuration with the old and refined structure.

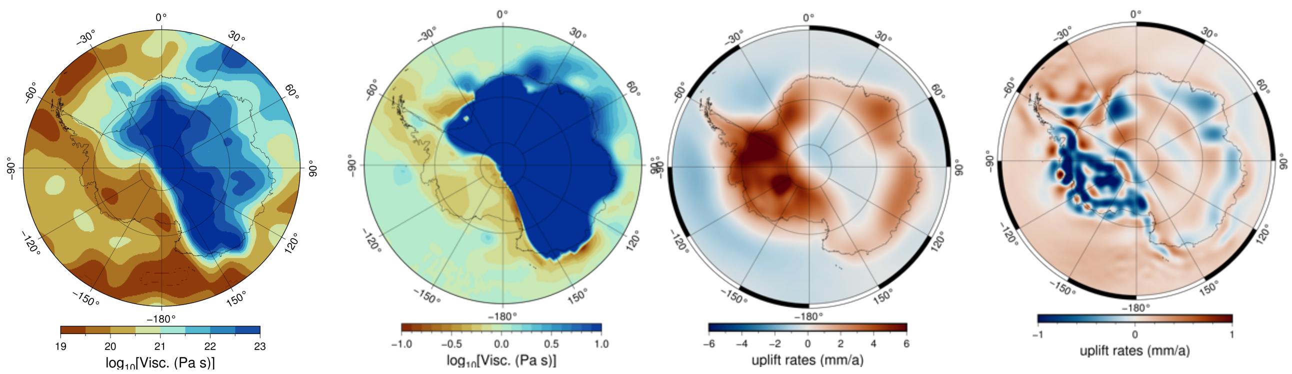

Figure 3: *Viscosity at 100 km depth and present day uplift rates of the refined Earth structure (left) and the respective differences to the global structure v_0.4_s16 (right).*

The vertical present day uplift rates of the 3D model ensemble are shown in Fig. 4 and represent a typical GIA pattern with highest uplift in North America (~16 mm/yr) and Fennoscandia / W-Antarctica (10 mm/yr). Subsidence is observed in forebulge regions around former glaciated areas. The standard deviation is ~2 mm/a in North America, Fennoscandia and W-Antarctica. The manuscript covering the validation of the model ensemble with observational data is in preparation (Boergens et al., in prep.).

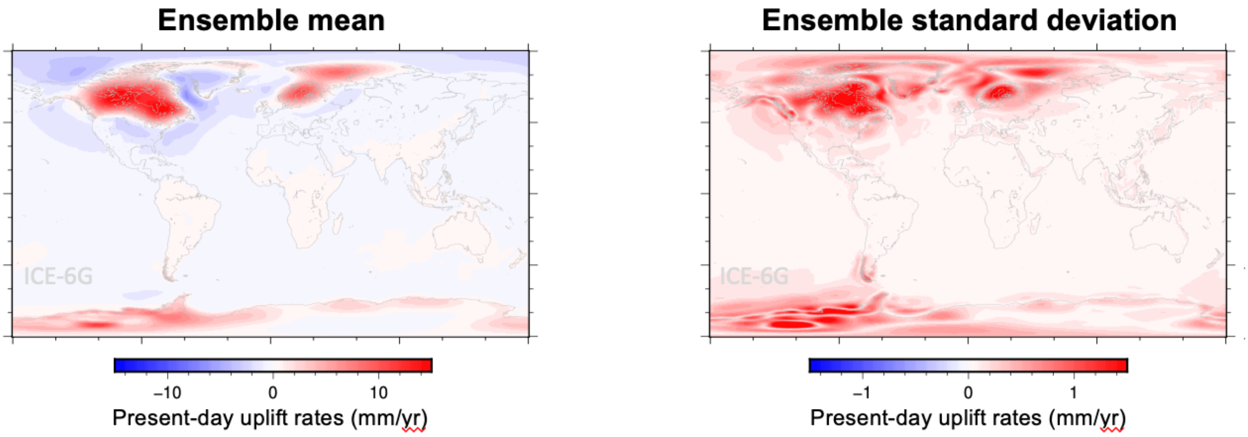

Figure 4: *Present day vertical uplift rates due to GIA for the ensemble mean and ensemble standard deviation*

The horizontal displacement rates for the GIA model ensemble reach up to 4 mm/a in the forebulge of North America (Fig. 5). The displacement rates are oriented towards the former ice sheet centers associated with the drag due to the back flow of mantle material acting on the lithospheric plates. Variability due to the considered Earth model ensemble is shown on the right.

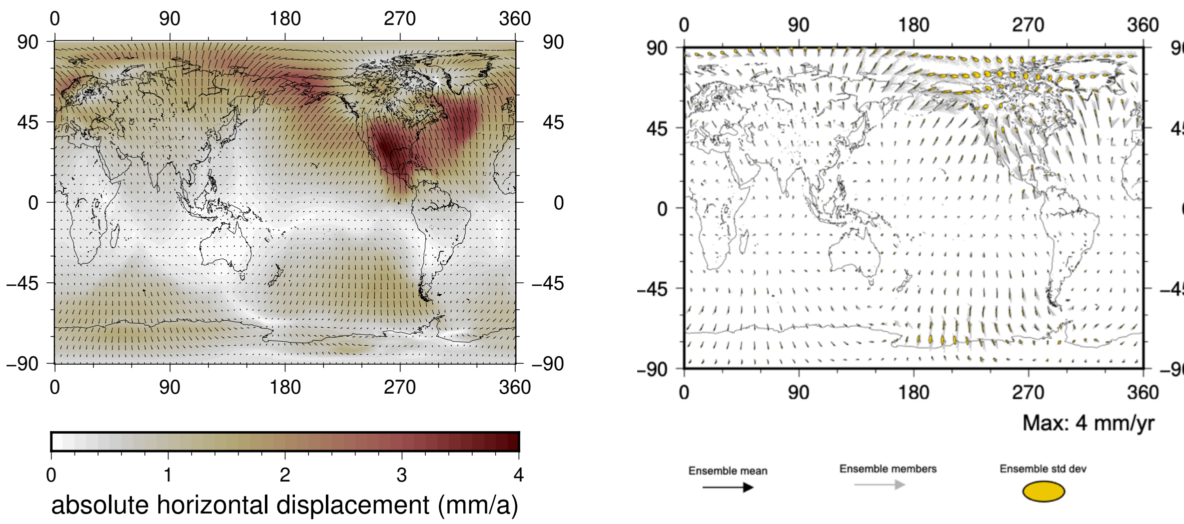

Figure 5: *Horizontal displacements due to GIA for the ensemble mean (left) and the ensemble members with standard deviation ellipse (right).*

To consider the effect on the plates' motion more realistically, we added plate boundaries in the viscosity structure as 200 km wide low viscosity zones (10^{20} Pa s) penetrating to the surface (purple lines in Fig. 6). Analysis of the resulting horizontal motion shows larger displacement rates at former ice-covered plates and smaller displacement rates of the surrounding plates. Furthermore, we observe abrupt velocity changes across plate boundaries due to the independent motion of the plates (Klemann et al., 2008).

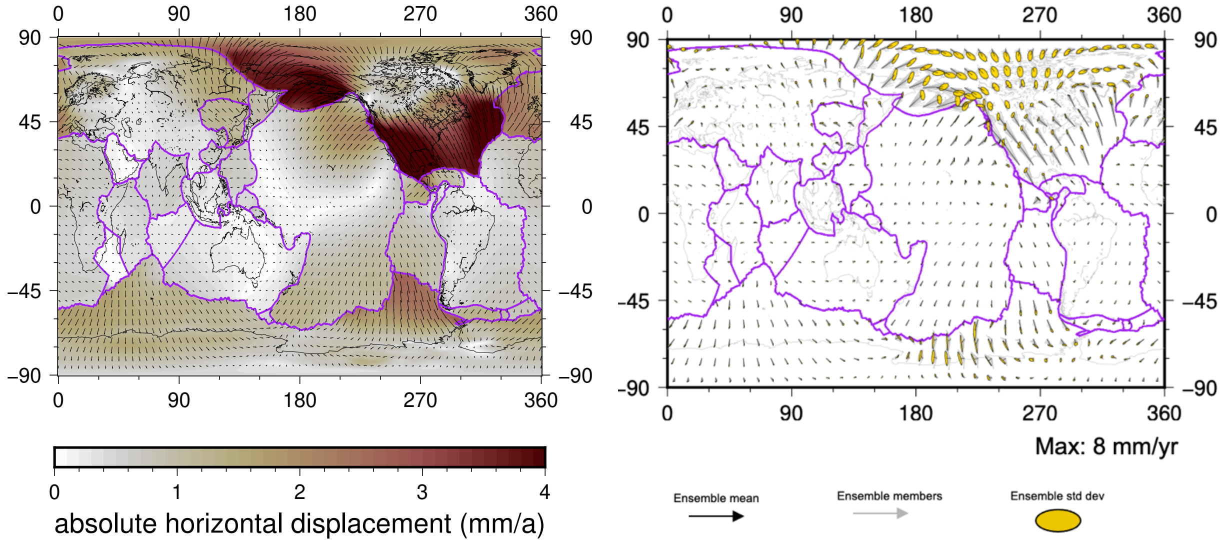

Figure 6: *Horizontal displacements due to GIA for the ensemble mean (left) and the ensemble members with standard deviation ellipse (right) for the models with implemented plate boundaries shown in purple.*

During 2022 the **AWI** has employed the fully coupled AWI-ESM2/PISM climate/ice-sheet model. Based on sensitivity studies from last year we conducted further studies regarding the last glacial inception. The simulations conducted so far have shown that the model cannot create an inception based on the modelled mean state of the climate. This problem is related to a persistent temperature bias in the model. By fixing the temperature bias, on the other hand, we were able to trigger the buildup of a large-scale ice sheet as will be outlined below. From 125 ka to 115 ka we find a cooling trend of about 0.4K/kyear at high latitudes and a warming by up to 1 K/kyear in the tropics (Fig. 7). These results fit to those found in other studies, with the exception of a too weak or absent cooling across Greenland and Northamerica in comparison to proxy records (cf. Bakker et al., 2014).

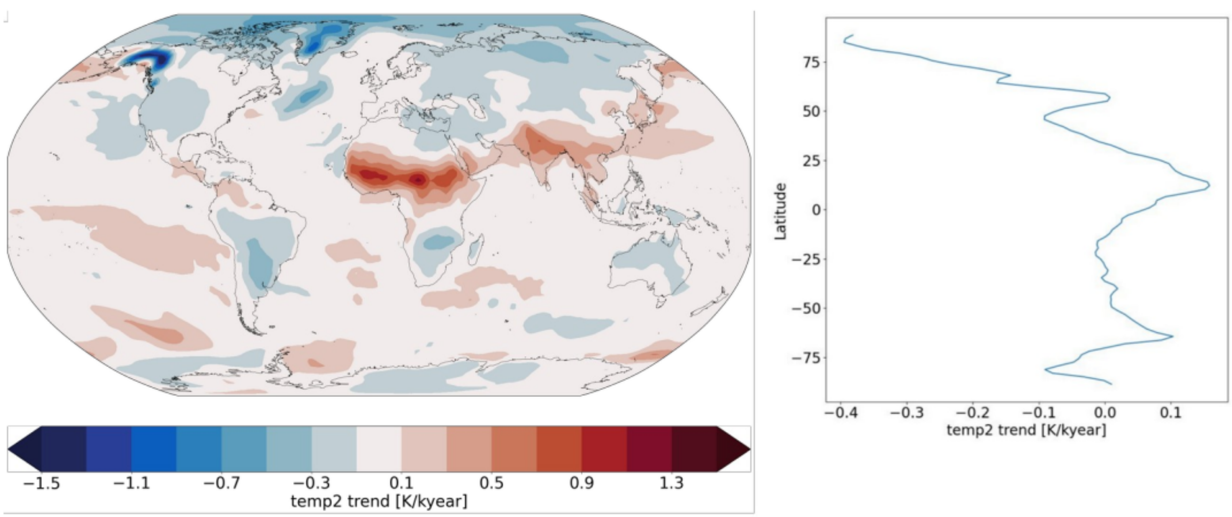

Figure 7: *Trend of near surface air temperature during the intervall of 125 ka to 115 ka; spatial distribution is shown on the left zonal mean is shown on the right.*

One part of the model bias was tackled by adjusting the coupling frequency between climate and ice sheet model to a shorter period of two model years. This avoided the filtering out, or dampening, of simulated extremely cold years in the climate forcing that is handed to the ice sheet model. Only the last model year is taken for the coupling so that the climate system has time to adjust to the modified ice sheet mask and topography data set. As in accelerated simulations the setup is still based on an asynchronous acceleration factor of 10, PISM is run with a chunk length of 20 model years.
A higher coupling frequency leads to less filtering of extremely cold years and therefore to a more accurate representation of the simulated climate in the atmospheric forcing that is handed over to the ice sheet model. Consequently, by employing a setup with higher coupling frequency we create a simulation that is less afflicted by bias in the successful triggering of glacial inception. This finding highlights the importance to run more simulations in an unaccelerated setup. From a scientific point of view we would like to avoid missing important key events regarding the establishment and stability of the simulated ice sheets. Consequently, for the coming allocation period, we apply for additional computational resources for non-accelerated simulations (see application document).

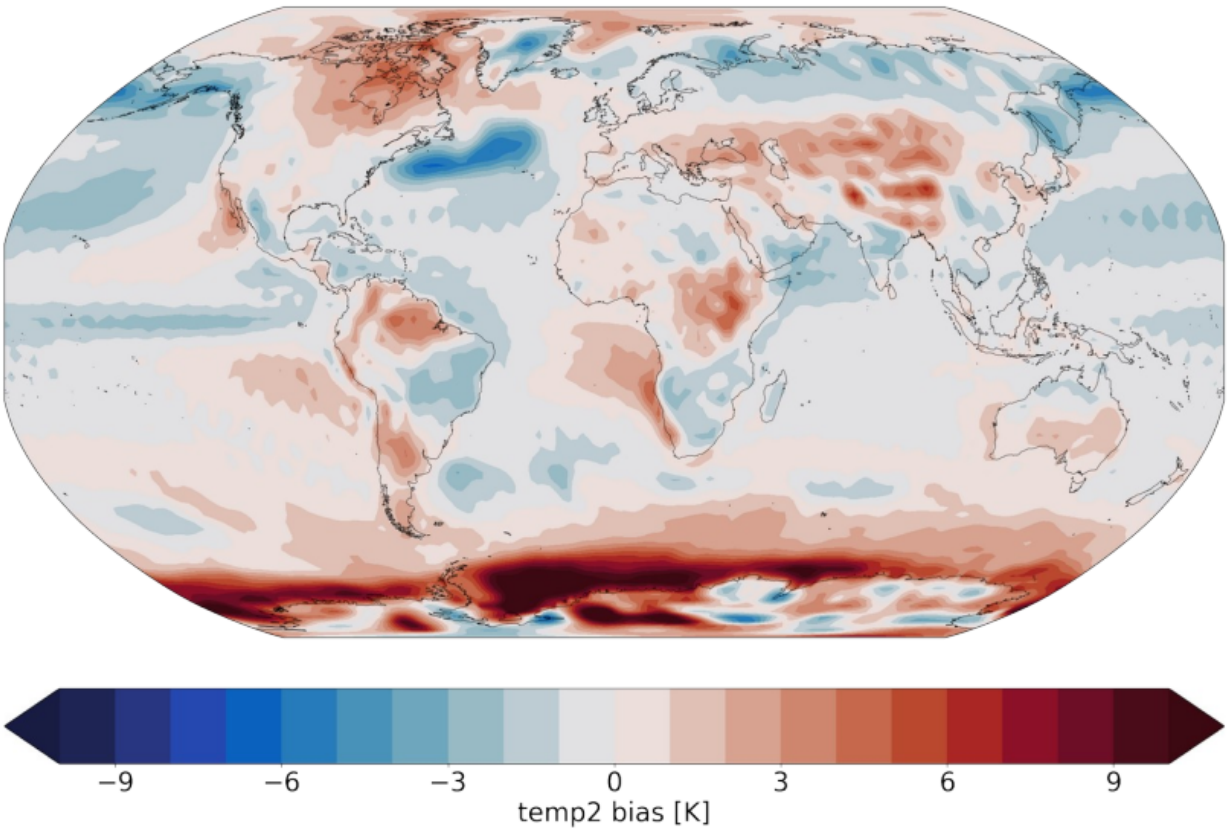

Figure 8: *Deviation of near surface air temperature in the AWI-ESM2 in comparison to reanalysis data (here: NCEP).*

A second problem that we found has been a general bias of near surface air temperature and precipitation in the model. We show below that the presence or absence of this bias is a factor that is critical to success or failure of glacial inception in the model. Figure 8 shows the deviation between simulated near surface air temperature in AWI-ESM2 and the same quantity derived from reanalysis data sets at comparable periods during recent time. In particular, in the northern part of North America, along Baffin Bay, the model is shown to be biased towards warmer temperatures, by about 3 K to 5 K, in comparison to the reanalysis data. On the other hand the model is too cold at the Cordillera. To overcome this bias in the mean state of the model in regions that are critical for inception we implemented an anomaly coupling that allows for a spatially modulated adjustment of temperature and precipitation in the atmospheric forcing that is handed over from the climate model to the ice sheet model. Figure 8 illustrates that a spatially-resolved adjustment of the forcing data is more advantageous than if instead a spatially uniform temperature adjustment was used. We tested the impact of the bias correction on inception in AWI-ESM2 by simulating the climate at 115 ka using various reanalysis data sets as a reference for bias correction. The magnitude and spatial distribution of the temperature correction term was derived by comparing results from a historical simulation with AWI-ESM2 to reanalysis data at comparable time intervals. Similarly we derived a correction for precipitation data. We found that when using NCEP reanalysis data as a reference for bias correction then we are indeed able to trigger large-scale glaciation across North America at 115 ka. With other reanalysis data sets we did not reach inception for this specific time interval (Figure 9 and 10). In the framework of coupled climate/ice-sheet simulations in PalMod we will therefore correct simulated near surface air temperature to reduce the bias in the climate model during the coupling of atmospheric forcing fields to the ice sheet model.

We must note that with NCEP as a reference for bias correction one can also trigger inception for the pre-industrial climate state. To overcome this problem the model is currently tuned towards refining ice-sheet sensitivity to atmospheric forcing. Consequently, in the framework of simulations „Extended integrations towards MIS 5.2“ that we propose for the coming allocation period, we aim to further explore the impact of different boundary conditions and reference data sets used for the bias correction on the transient evolution of climate and of ice sheets in the period from 125 ka to 86 ka.

As a general result of our work with coupled climate/ice-sheet simulations in the ongoing allocation period we can highlight that the model shows the necessary sensitivity to climate forcing to trigger inception. Whether or not inception is successful on the other hand largely depends on the mean state of the simulated climate. The latter suffers from biases that are corrected by retuning the ice sheet model and applying forcing correction in conjecture with a reduced coupling step as outlined above.

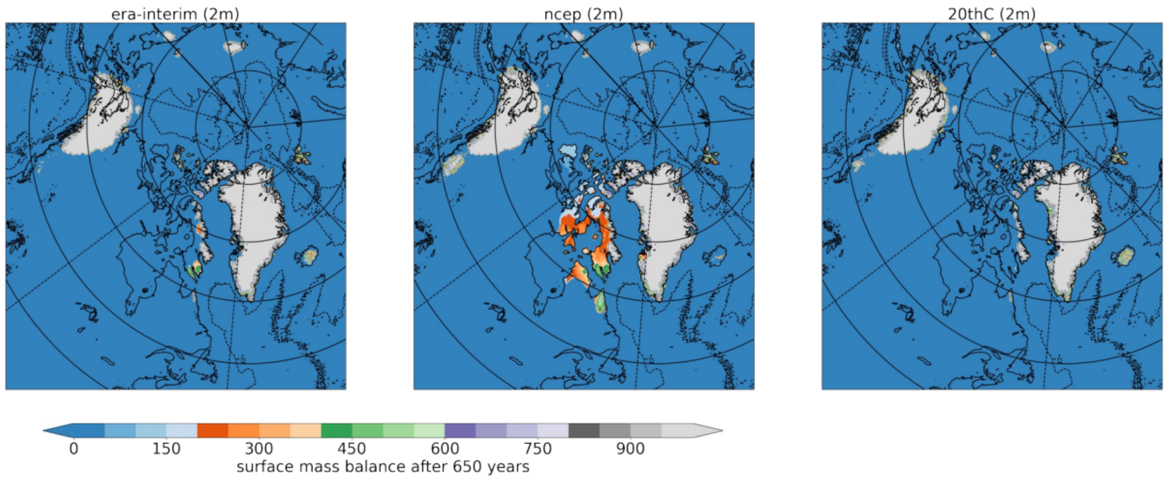

Figure 9: *Dependence of the thickness of the simulated ice sheet after 650 model years employing anomaly coupling using different reanalysis data sets as reference for the bias correction.*

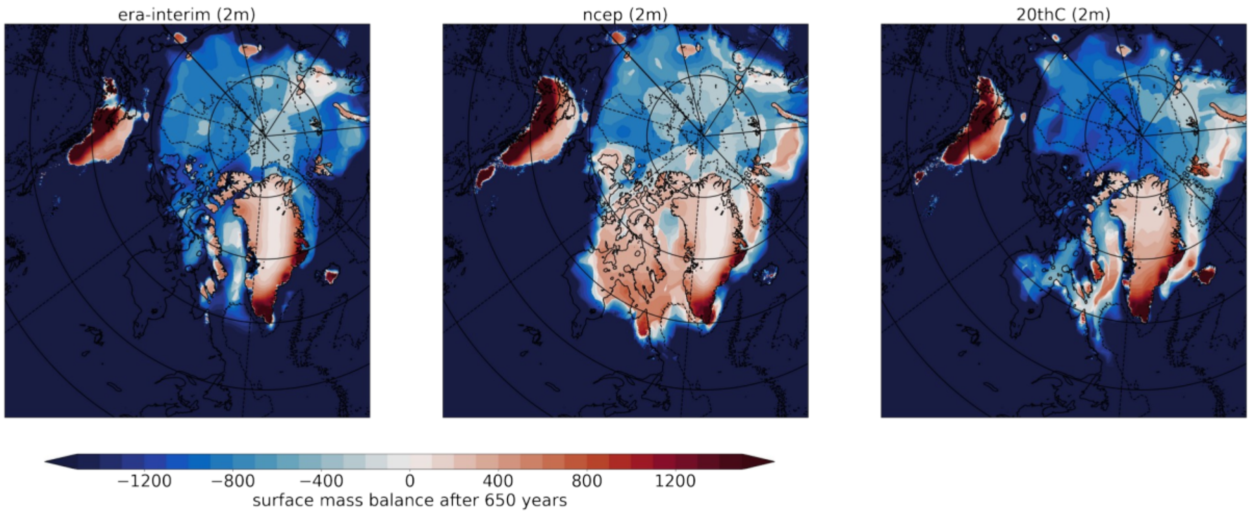

Figure 10: *As Figure 9, but showing surface mass balance instead of thickness of the simulated ice sheet.*

A further technical development that has been addressed during the ongoing allocation period is implementation of a bihemispheric setup for the coupled climate/ice-sheet system. This enables having ice sheets being simultaneously simulated in both hemispheres in the coupled AWI-ESM2/PISM system. The advantage of our chosen bihemispheric setup is that the model system can be configured independently for both hemispheres, allowing us to consider specific differences of ice sheet characteristics between Antarctica (for example presence of a large ice shelf) and Northern Hemisphere.

With regard to our research of the phase space analysis of MIS3 we found that the model simulated a too strong AMOC among other discrepancies with regard to MIS3 climate. The model has been retuned based on modification of the mixing scheme. In the framework of a collaboration with WG3 better results were derived. Yet, as WG1 is currently, and in the future, lacking a dedicated person to work on this specific topic, we will unfortunately not be able to further research this field.

During 2023 we will further strengthen the collaboration with WG3 in that we combine our modelling efforts over the last deglaciation and into the future. WG1 at AWI will build on the work done in WG3 at AWI in simulating the last deglaciation from LGM until today with an isotope-enabled model. WG1 will explore the sensitivity of the physical climate system based on pessimistic and optimistic trajectories of future emissions of greenhouse gases. The effect will be quantified by comparison to an unperturbed transient baseline simulation (see application for computing time by WG3 and WG1 as well as the report by WG3).
We note that the switch from Mistral to Levante has also at AWI led to a considerable delay of our work that was planned for allocation period 2022. Furthermore, the switch of the HPC, as well as model development and improvement outlined above, necessitates that various simulations are a) redone on the new HPC for comparability b) redone with the improved climate/ice-sheet system AWI-ESM2 in order to reach our scientific goals.

1.2 Publications and References

Bagge, M., Klemann, V., Steinberger, B., Latinović, M., and Thomas, M. (2021). *Glacial-isostatic adjustment models using geodynamically constrained 3D Earth structures.* Geochemistry Geophysics Geosystems, 22, e2021GC009853. https://doi.org/10.1029/2021GC009853

Bagge, M., Klemann, V., Steinberger, B., Latinović, M., Thomas, M. (2020). *3D Earth structures for glacial-isostatic adjustment models*. V. 1.0. GFZ Data Services. https://doi.org/10.5880/GFZ.1.3.2020.004

Bakker, P., Masson-Delmotte, V., Martrat, B., Charbit, S., Renssen, H., Gröger, M., ... & Varma, V. (2014). *Temperature trends during the Present and Last Interglacial periods–a multi-model-data comparison*. Quaternary Science Reviews, 99, 224-243.

Boergens, E., Bagge, M., Balidakis, K., Klemann, V., Dobslaw, H., *Optimising GIA Model Parametrisation: A New Validation Method for Modelled Present-Day GIA Uplift Rates against a Space Geodetic Data Set*. (in prep.)

Haeger, C., Petrunin, A. G., & Kaban, M.K. (2022). *Geothermal heat flow and thermal structure of the Antarctic lithosphere*. Geochemistry, Geophysics, Geosystems. (accepted)

Klemann, V., Martinec, Z., Ivins, E. R. (2008). *Glacial isostasy and plate motions*. Journal of Geodynamics, 46, 95-109, https://doi.org/10.1016/j.jog.2008.04.005

Steinberger, B. (2016). *Topography caused by mantle density variations: Observation-based estimates and models derived from tomography and lithosphere thickness*. Geophysical Journal International, 205(1), 604–621. https://doi.org/10.1093/gji/ggw040

Steinberger, B., & Calderwood, A. R. (2006). *Models of large-scale viscous flow in the Earth's mantle with constraints from mineral physics and surface observations*. Geophysical Journal International, 167(3), 1461–1481.

2. Project 1030 / WG2

Project title: PalMod WG2 - Biogeochemistry
Project lead: V.Brovkin (MPI-M), P. Köhler (AWI)
Subproject lead: P.Köhler (AWI), M.Claussen (MPI-M), B.Schneider (CAU Kiel), T.Ilyina (MPI-M), T.Kleinen (MPI-M), B.Steil (MPI-C), A.Paul(MARUM)
Allocation period: 01.01.2022 – 30.09.20232

2.1 Report on resources used in 2022

WG2 of PalMod aims at understanding and quantifying feedbacks between biogeochemistry and climate during glacial cycles. Three work packages are focusing on the marine carbon cycle, terrestrial processes, and the CH_4 cycle. Scientific challenges include reproducing the glacial CO_2 cycle with comprehensive ESMs, understanding of rapid changes in atmospheric greenhouse gas concentrations during abrupt climate changes, and reconstructing the atmospheric lifetime of CH_4 using a coupled atmospheric chemistry model.

PalMod WG2 contains work packages WP2.1 "Marine carbon cycle", WP2.2 "Terrestrial carbon cycle", and WP2.3 "Methane cycle". During the reporting period all work packages requested computation time from DKRZ.

WP 2.1 "Marine carbon cycle", CAU Kiel

Preface

Due to long queue times on Mistral, we had decided in late 2021 to wait with the start of the transient MPI-ESM simulations until Levante was available.

Moreover, we had moved the CLIMBER-X code from Mistral to our local computational facilities at CAU by the beginning of 2022. Therefore, we used almost no computing time on Mistral in January to May 2022. When Levante became available and initial challenges of porting MPI-ESM were solved, our transition to Levante was further delayed by

1) other duties at that time that we could already efficiently work on, such as the inclusion of the M4AGO-scheme in CLIMBER-X,
2) 2) the summer break, and
3) 3) a subsequent Corona infection. We expect to start transient MPI-ESM simulations and to use our allocated computing time on Levante in the remaining quarter of 2022.

Report in detail

In late 2021 we extended selected LGM and pre-industrial simulations with particle ballasting, in preparation for a comparison with M4AGO simulations performed at MPI-M in Hamburg. Due to long queue times on Mistral during that time, we decided to wait for Levante to start with the originally planned transient simulations.

In the meantime, we used some of the remaining computing time on Mistral for PI and LGM equilibrium simulations with CLIMBER-X to estimate the effect of particle ballasting on glacial-interglacial pCO_2, and to extend the particle ballasting parameterization to include the effect of viscosity (Fig. 1).

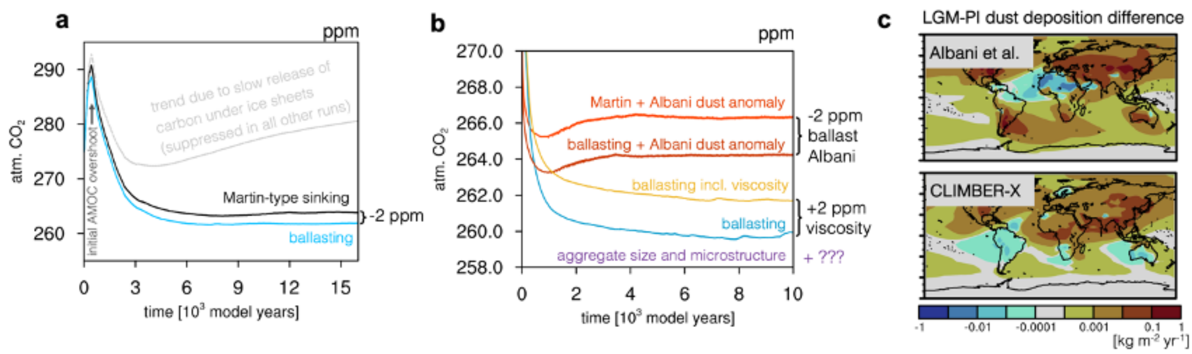

Fig. 1: LGM-simulations with CLIMBER-X. a) Prognostic atmospheric CO_2 concentration in CLIMBER-X simulations with LGM boundary conditions with prescribed sinking speeds (black: Martin-type sinking) and with particle ballasting (blue); the initial rise in pCO_2 is due to the transitionally stronger Atlantic meridional overturning circulation (AMOC); the release of carbon from underneath the instantaneously prescribed LGM ice sheets would usually lead to a long-term, positive pCO_2 trend (gray), which is suppressed in all other simulations by increasing the respective release-timescale from 10^4 to 10^9 years. b) Prognostic atmospheric pCO_2 in sensitivity runs with prescribed LGM-PI dust anomaly by Albani et al. (2016) (red and orange, with and without ballasting, respectively) compared to the run with interactively calculated CLIMBER-X dust (blue) and including the effect of larger seawater viscosity during the LGM (yellow). To our knowledge, potential effects of aggregate size distribution and microstructure have not yet been quantified (purple question marks). c) Mean LGM-PI dust deposition anomaly according to Albani et al. (2016, upper panel) and as interactively calculated in CLIMBER-X (lower panel).

In addition, particle ballasting effects were quantified in transient simulations of the last glacial inception. As for the LGM-PI anomaly experiments, the ballasting effects during the inception are usually small. However, these small effects can in some cases be amplified, e.g., by Atlantic meridional overturning circulation (AMOC) changes that are sensitive to boundary conditions affected by the carbon cycle (Fig. 2). Although this effect is not yet well understood, it highlights the potential usefulness of ensemble simulations to estimate the robustness of model results.

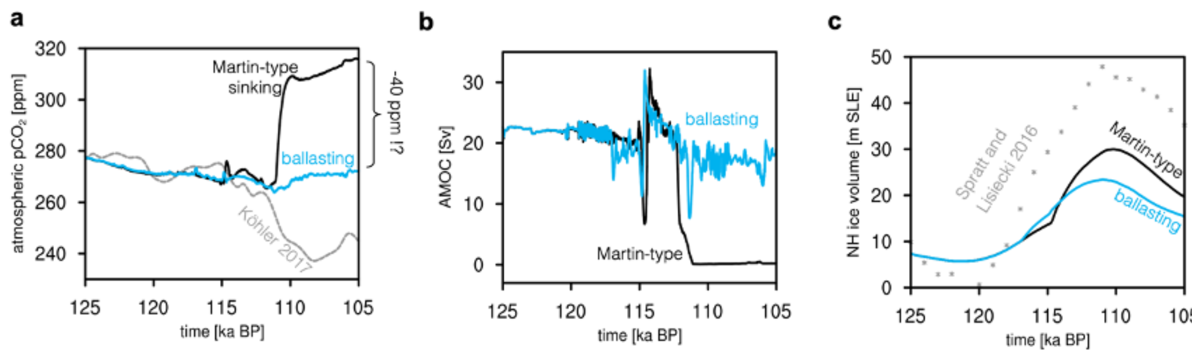

Fig. 2: Transient simulations of the last glacial inception using CLIMBER-X. a) Atmospheric pCO_2-for simulations with (blue) and without (black) ballasting effect compared to reconstructions (Köhler et al. 2017, gray) b) Maximum of the AMOC streamfunction in Sverdrups (1 Sv = $10^6 m^3/s$), and c) Northern Hemisphere ice volume for the simulations with (blue) and without (black) ballasting effect in meters sea-level equivalent (m SLE) compared to sea-level reconstructions (Spratt and Lisiecki 2016; gray stars).

With respect to MPI-ESM, we are currently in the process of transitioning from Mistral to Levante and are planning to start transient experiments with particle ballasting within the remaining quarter of this year.

WP 2.1 "Marine carbon cycle", MPI-M

Preface

In Jan-May of 2022, we used all computing time allocated to our subproject on Mistral. Specifically, we used 70844 node hours, more than that granted to our subproject (57257 node hours for Jan-June, which is 19.4% of the allocated resources to project bm1030).
In March-June of 2022, we did not run simulations on Levante because of the technical work related to porting MPI-ESM to Levante, adjusting environment settings, pre-/post-processing scripts and model scripts. In July-Sep, we used 9465 node hours on Levante (57% out of 16665 node hours allocated to our subproject) because of the ongoing adjustment and testing of the topography scripts for the transient simulations. We expect to start more simulations in the last quarter of 2022 when the transient runs can run smoothly on Levante.

Report in detail

1. *Impact of model tuning on the deglaciation variations of air-sea CO_2 flux and ocean biogeochemistry*

To better constrain the deglaciation variations in ocean biogeochemistry, we conducted a new transient deglaciation simulation with different model tuning (hereafter "model_T2"), and we compared it to the previous deglaciation simulation (model_T1) and proxy data. In model_T2, the cloud parameters were tuned by WG1 to improve the glacial AMOC state; several marine biogeochemical parameters (e.g. organic matter sinking speed, iron bio-availability) were tuned by our subproject to improve the comparison to present-day ocean biogeochemical observations.
We found that the timing of the $\delta^{13}C$ decline in both model_T1 and model_T2 is not represented because the timing of AMOC shoaling/weakening is not consistent with the data (Fig 1a). model_T2 improves the magnitude of the $\delta^{13}C$ decline because of a larger organic matter export in high latitudes, which leads to a larger change in the regenerated nutrients and carbon.
AMOC weakening can induce CO_2 outgassing because from the beginning to the peak of the meltwater pulse, reduction of primary production increases surface DIC (consistent with previous hosing experiments in Schmittner et al. 2015); from the peak to the end of the meltwater pulse, rising SST dominates sea surface pCO_2 rise. model_T2 simulates more episodes and larger amplitudes of AMOC weakening (Fig 1b), thus favours CO_2 outgassing (Fig 1c). Therefore, our future transient deglaciation simulations will be based on model_T2.

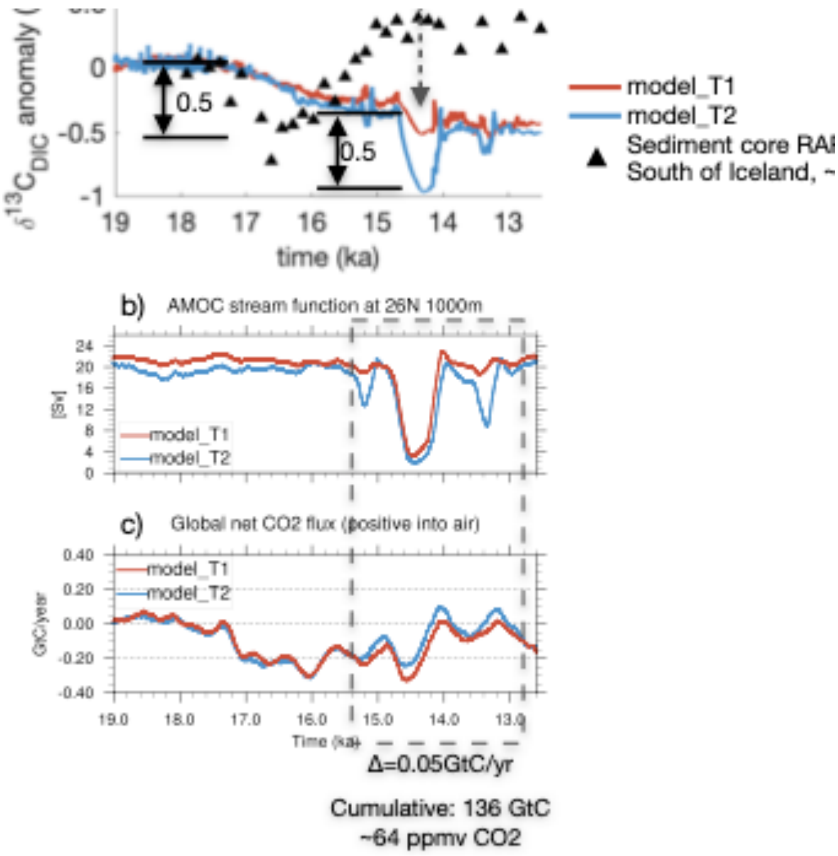

Fig. 1: (a) Comparison of simulated δ13C anomaly to data from core RAPiD_17 in the North Atlantic Ocean. δ13C data is from Jonkers et al. (2020), and age is generated with PaleoDataView (Langner and Mulitza, 2019). (b) AMOC strength at 26N 1000m and (c) global net air-ocean CO2 flux during the early deglaciation in MPI-ESM.

2. *Model development on prognostic CO2 setup*

The current prescribed-CO_2 setup (model_T1 and model_T2) cannot simulate deglacial CO_2 outgassing because the air-sea CO_2 flux is mainly forced by prescribed CO_2 rather than internally evolved mechanisms. This emphasises the urgent need for a prognostic CO_2 setup. To complete the existing prognostic CO_2 setup, we further developed the prognostic atmospheric carbon isotope module, in collaboration with WP2.3, and coupled it with the oceanic carbon isotope module (Liu et al. 2021). We have tested prognostic ^{13}C for the pre-industrial period. The seasonal variability of the atmospheric $\delta^{13}C$ well captures that shown in the present-day observations, suggesting a successful implementation. In the last quarter of 2022, we will test and adjust parameters for prognostic ^{14}C.

3) Impact of circulation and marine particle sinking on glacial oceanic biogeochemistry

To advance the understanding of marine carbon and nutrient cycling during LGM, we conduct LGM and PI time-slice simulations using the MPI-ESM and compare them to marine proxy data. We carry out sensitivity studies with different circulation states achieved by tuning vertical background diffusivity (hereafter “strong-mix” and “weak-mix” model; strong-mix employs the same physical model as model_T2 in section 1) and with different complexities of marine biogenic particle sinking (Martin scheme and M4AGO scheme; Maerz et al., 2020). All 4 model set-ups well represent the PI ocean physics and biogeochemistry.

We found that weak-mix yields a shallower and weaker LGM AMOC than strong-mix (Fig 2a, 2c) due to a more southward ice edge in the North Atlantic which prohibits deep convection. In weak-mix, the LGM southern-sourced water (SSW) consists of a larger fraction of the deep waters than PI (Fig 2c, 2d). This leads to an older LGM seawater age in the Atlantic and a younger seawater age in the Pacific (not shown). In strong-mix, ^{14}C ventilation age is generally larger during LGM than PI, in agreement with data (Fig 2e, 2f, 2i, 2j), mainly due to more limited air-sea gas exchange under lower LGM pCO_2 and larger sea ice cover. Weak-mix shows a better agreement to ^{14}C ventilation age data than strong-mix in the Atlantic but a worse agreement in the Pacific because of the change of water mass composition (Fig 2e-2j).

$\Delta\delta^{13}C$ data in the Atlantic Ocean is better captured by weak-mix (Fig 2k, 2m, 2o) owing to a stronger deep-ocean stratification. The M4AGO scheme yields better agreement with $\Delta\delta^{13}C$ data in the Southern Ocean and Atlantic due to a larger LGM-PI increase in the marine aggregate sinking speed and organic matter export (not shown). Hence the impact of different sinking schemes is larger for weak-mix. Weak-mix also improves comparison to ΔCO_3^{2-} data in the Atlantic (Fig 2q, 2s, 2u) owing to the sequestration of more respired carbon during LGM.

We have presented the above simulations and analysis at the 14th International Conference on Paleoceanography (Bergen, Aug 29 – Sep 02, 2022). We are currently preparing a manuscript based on the these results.

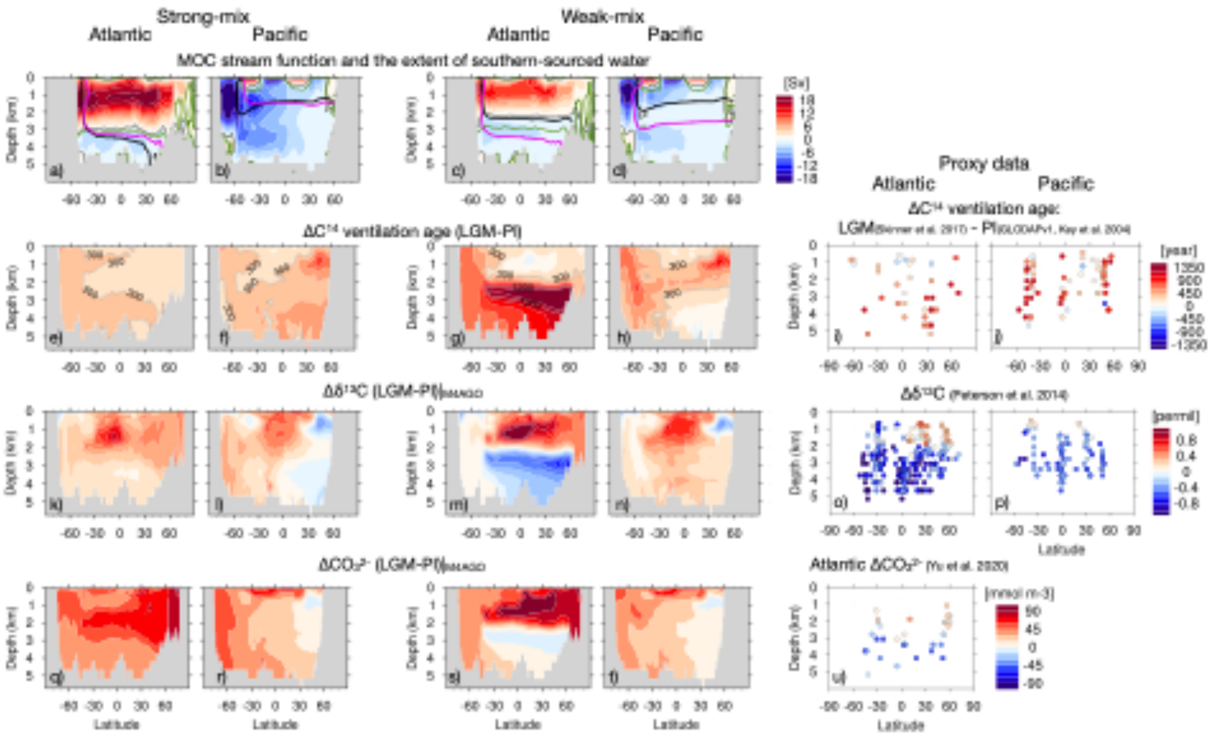

Fig. 2: The LGM meridional overturning circulation stream function (a-d), ^{14}C ventilation age (LGM-PI) change (e-j), the $\delta^{13}C$ (LGM-PI) changes (k-p) and the CO_3^{2-} (LGM-PI) changes (q-u) for the strong-mix model (leftmost two columns), weak-mix model (middle two columns) and the proxy data (rightmost two columns). In panels a-d, the grey and green lines show the NADW/AAWB boundary for LGM and PI, respectively; the black and magenta lines show the extent of south-sourced water (SSW) for LGM and PI, respectively.

WP2.2 "Terrestrial Carbon Cycle", WP 2.3 "Methane cycle" (MPI-M)

Preface

Unfortunately, we were able to use only a fraction of the computation time we had applied for. This was largely due to the unavailability of sufficient computing resources, which severely delayed progress during the first half of 2022: Due to the extremely slow turnover we were able to achieve on Mistral in late 2021 and early 2022, we were very slow in preparing the initial conditions required for the intended experiments (10000-year model spinup at 125 ka BP conditions). Furthermore, when Levante was opened to the public, MPI-ESM and especially the vital scripting allowing the use of the model under changing sea level and glacier masks were not yet available to run "out of the box" on Levante, requiring several weeks work for code changes and testing, with the final bug stemming from software unavailability only being resolved in late June.

Report in detail

1) **WP2.2 "Terrestrial Carbon Cycle" (MPI-M)**

For 2022, WP2.2 had planned to work on the recently developed representation of carbon isotopes in JSBACH, performing transient glacial inception and deglaciation experiments in order to investigate carbon isotope sensitivity to uncertain model parameters. These experiments are still planned for the second half of 2022, but model development is only now at a point where these can be undertaken, as neither mistral nor levante were available for crucial development test experiments in late 2021 and early 2022.

By now, the isotopes code for the terrestrial carbon cycle has been thoroughly tested and appears to be working nicely, as demonstrated in Fig. 2.2-1.

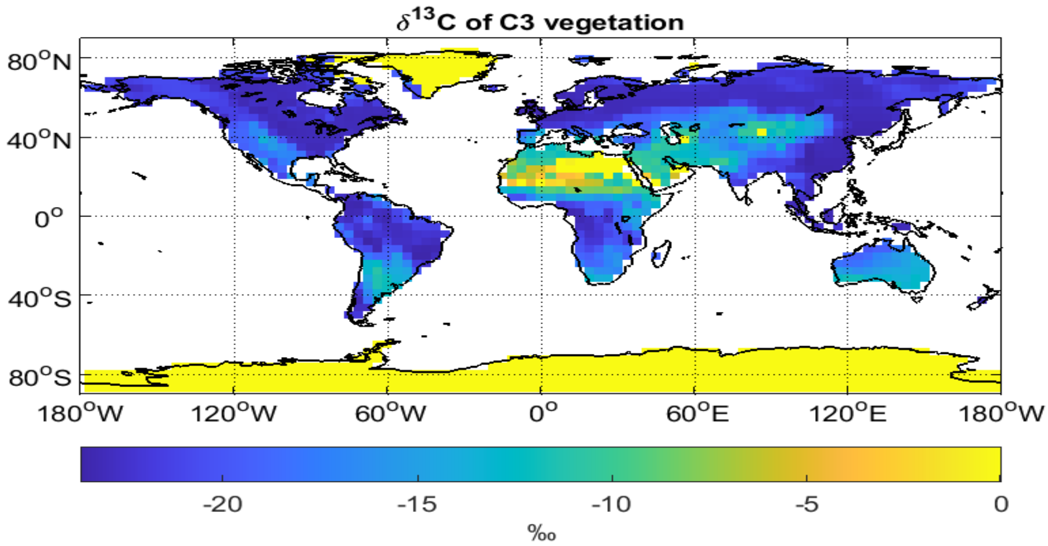

Fig. 2.2-1: δ13C (carbon isotope ratio in comparison to standard) of carbon in C3 vegetation.

Using this baseline, we will finally be able to perform the sensitivity experiments originally planned for earlier in 2022.
We did, however, perform an initial glacial inception experiment together with WP2.3 to insure the model works technically and to understand climate changes during the inception.

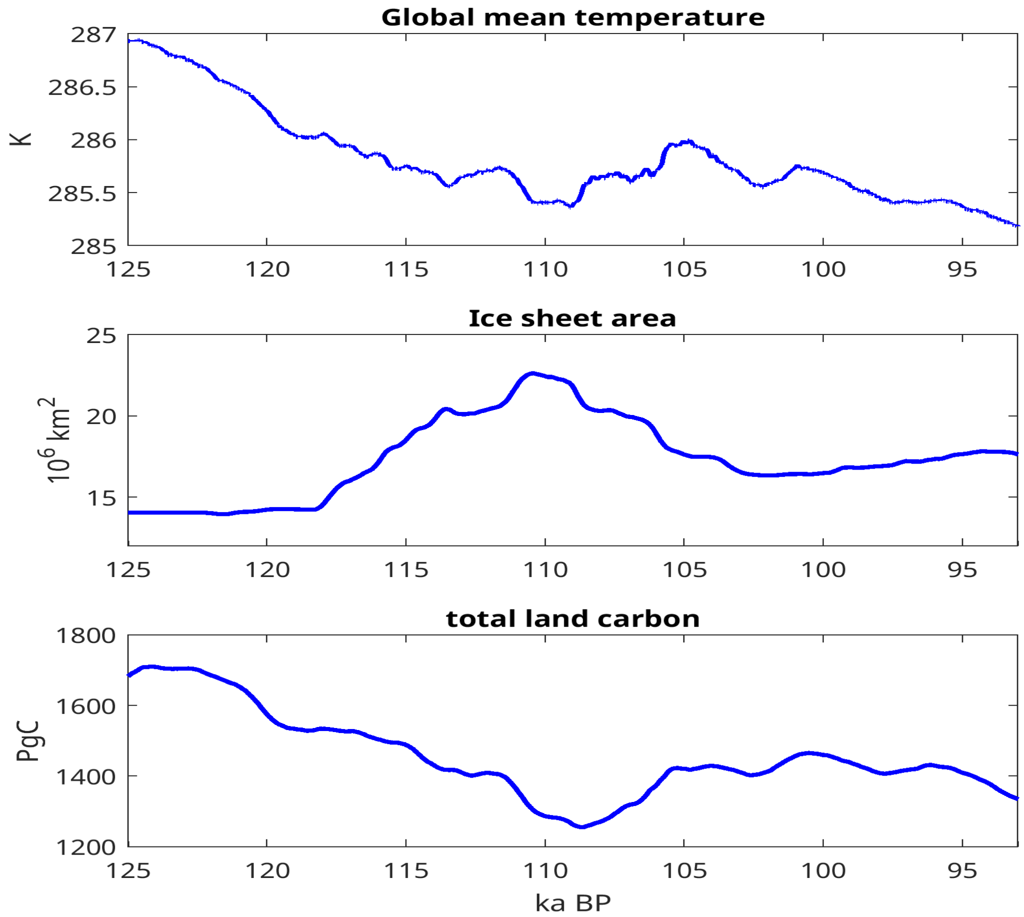

Fig. 2.2-2: Glacial inception test: global mean temperature (top), ice sheet area (centre) and total land carbon (bottom) in glacial inception test.

As shown in Fig. 2.2-2, conditions become continuously colder during the Eemian, from 125 ka BP to 118 ka BP. At 118 ka BP, inception sets in, and the ice sheet area grows, while temperatures keep falling. The ice sheets reach an initial peak at 110 ka BP and shrink again afterwards, while temperatures reach an initial minimum at that time.Climate slightly warms again afterwards, but the increase in temperature is far less pronounced than the decreae in ice sheet area.Finally, land carbon drops continuously from 125 ka BP to 110 ka BP, recovering slightly over the next 5000 years, but not reaching interglacial levels again.

Further experiments performed in 2022 aimed at clarifying some issues with the “Deglacial forest conundrum” described in last year’s report. Our deglaciation experiments, when compared to vegetation reconstructions, show a significant difference in vegetation, especially forest, development, with forested area increasing substantially earlier in the model than in reconstructions (Fig. 2.2-3).

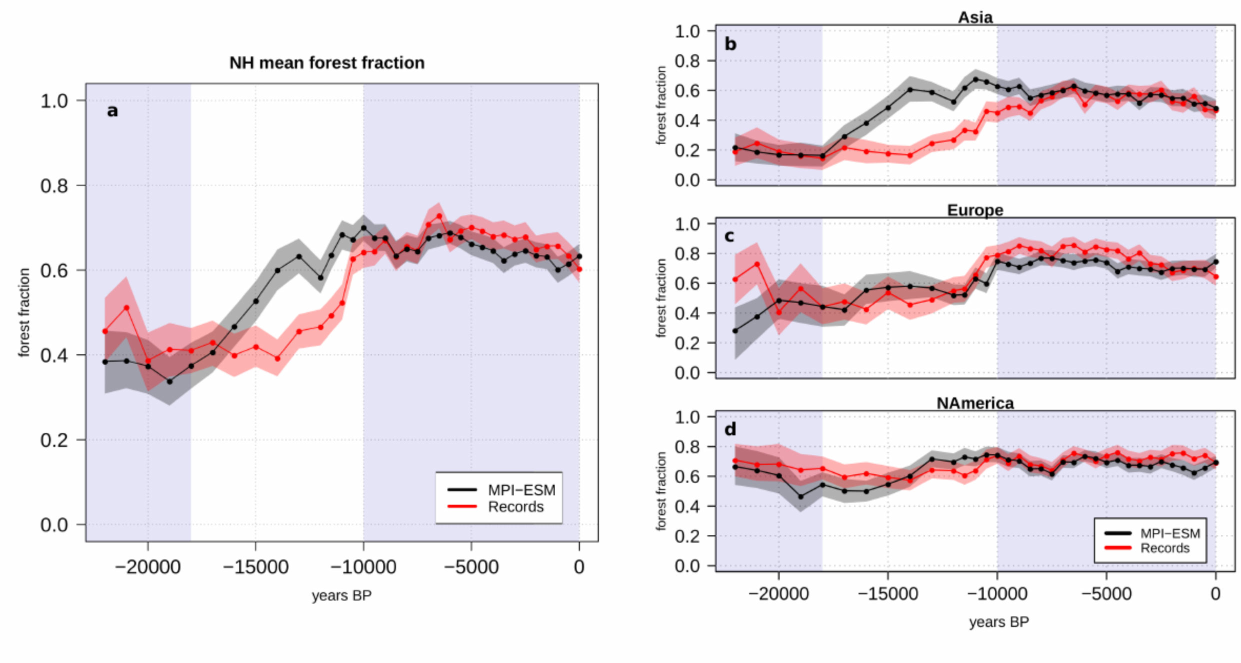

Fig. 2.2-3: The deglacial forest conundrum: NH forest cover expands significantly earlier than indicated by vegetation reconstructions. Pronounced for Asia, negligible on other continents.

As we indicate in our corresponding Publication (Dallmeyer et al., in press), climate indicators that are not based on plant pollen compare rather favorably with model results, thus indicating that the source of the discrepancy is not the climate model, but rather the assumptions in the vegetation development.

We performed a number of sensitivity experiments, for example with fixed vegetation in order to resolve this issue, but haven't yet solved it — which we will attempt to do in 2023.

2) WP 2.3 "Methane cycle" (MPI-M)

In 2022, we had planned on investigating the methane cycle during glacial inception and during MIS 3. However, due to the unavailability of mistral in late 2021 (computer overloaded by very large experiments, reducing our turnover from 700 yrs/day to less than 50) and in early 2022 (regular crashes due to node failures) we were not able to perform the initial tests required to begin these experiments until after Levante had been opened and all the porting of MPIESM and scripting infrastructure had taken place. This was an especially heavy load on WP2.3, as we were the ones having the required expertise to finalise porting the code to Levante, thus making it impossible to work on other things.

We did, however, manage to finalise the publication on atmospheric methane during the deglaciation that we had worked on previously, see reports from last year and the year before, this has recently been submitted to Climate of the Past (Kleinen et al., in Review).

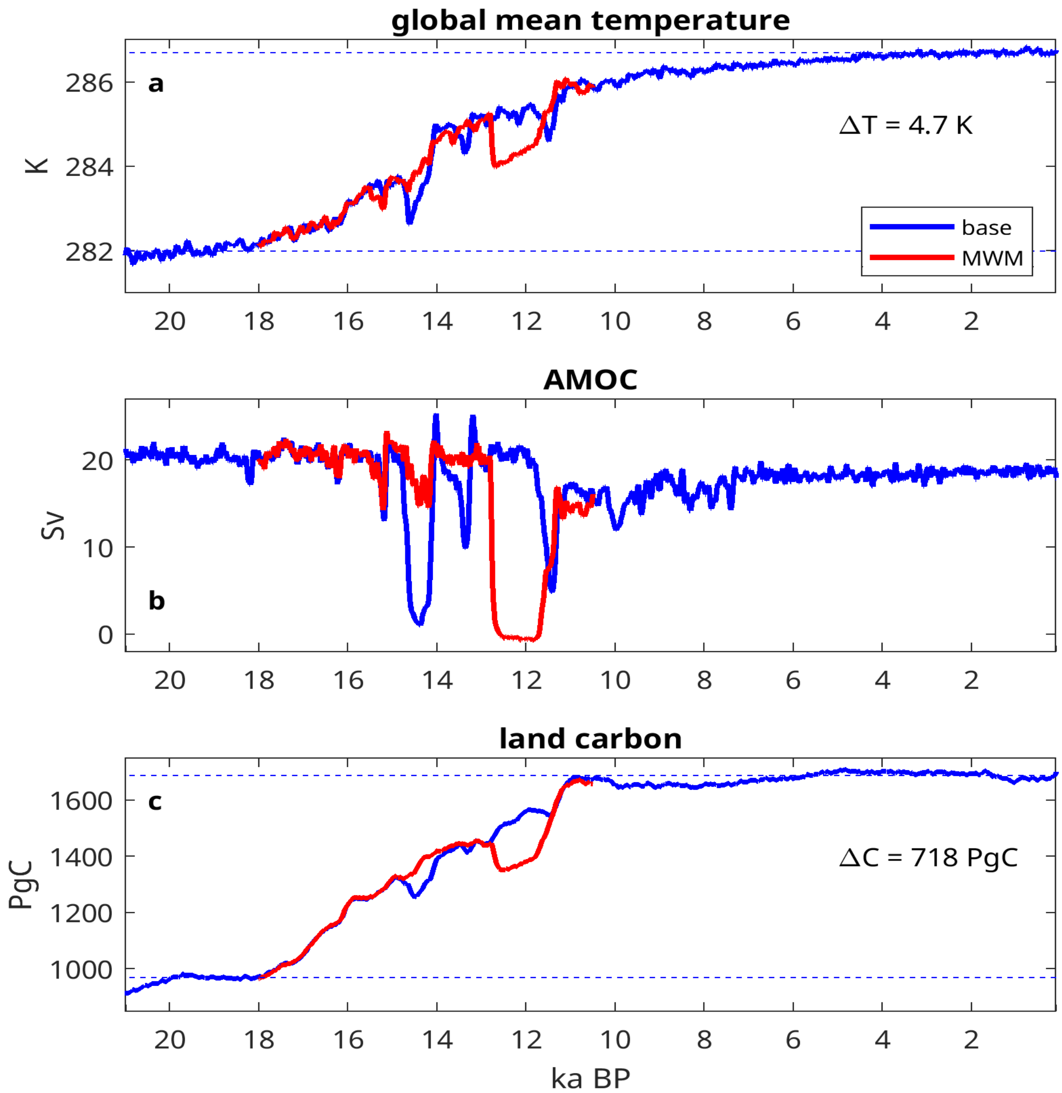

Fig. 2.3-1: Climate during the deglaciation, global mean temperature, AMOC overturning and total land C storage.

Especially interesting here was the fact that we were able to shed new light on the major climatic transitions during the deglaciation, especially the Bolling-Allerod — Younger Dryas transition at 12.8 ka BP. We addressed this by performing dedicated perturbation experiments, modifying the meltwater release from Laurentide ice sheet melt, shown in red in Fig. 2.3-1.

Using these experiments, we were able to get very close to our aim, understanding the deglacial evolution of methane in the climate system (Fig. 2.3-2).

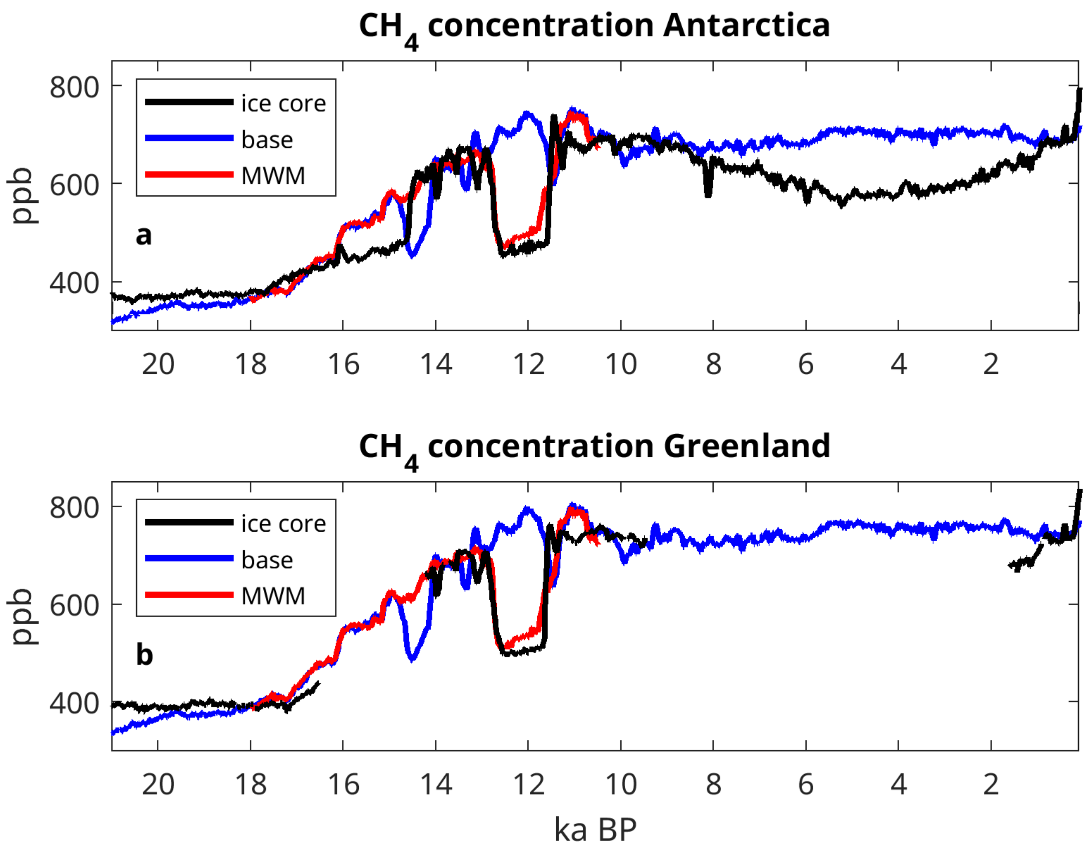

Fig. 2.3-2: Atmospheric methane over Antarctica (top) and Greenland (bottom) in model experiments (blue, red) and ice core data (black).

Despite the overall delays due to unavailability of computing resources, we were able to perform an initial glacial inception experiment, starting in the Eemian at 125 ka BP and integrating the model forward in time until 93 ka BP (Fig. 2.3-3, also Fig. 2.2-2 for further climate characteristics).

Here, as during the deglaciation, atmospheric CH_4 generally follows the changes in terrestrial fluxes, which are closely coupled to temperature and atmospheric CO_2. We will need to revisit this initial experiment, though, as atmospheric CH_4 was substantially higher than in ice core data, implying a need for further model tuning.

Unfortunately, we were able to use only a fraction of the computation time we had applied for. This was largely due to the unavailability of sufficient computing resources, which severely delayed progress during the first half of 2022: Due to the extremely slow turnover we were able to achieve on Mistral in late 2021 and early 2022, we were very slow in preparing the initial conditions required for the intended experiments (10000 year model spinup at 125 ka BP conditions). Furthermore, when Levante was opened to the public, MPI-ESM and especially the vital scripting allowing the use of the model under changing sea level and glacier masks were not yet available to run “out of the box” on Levante, requiring several weeks work for code changes and testing, with the final bug stemming from software unavailability only being resolved in late June.

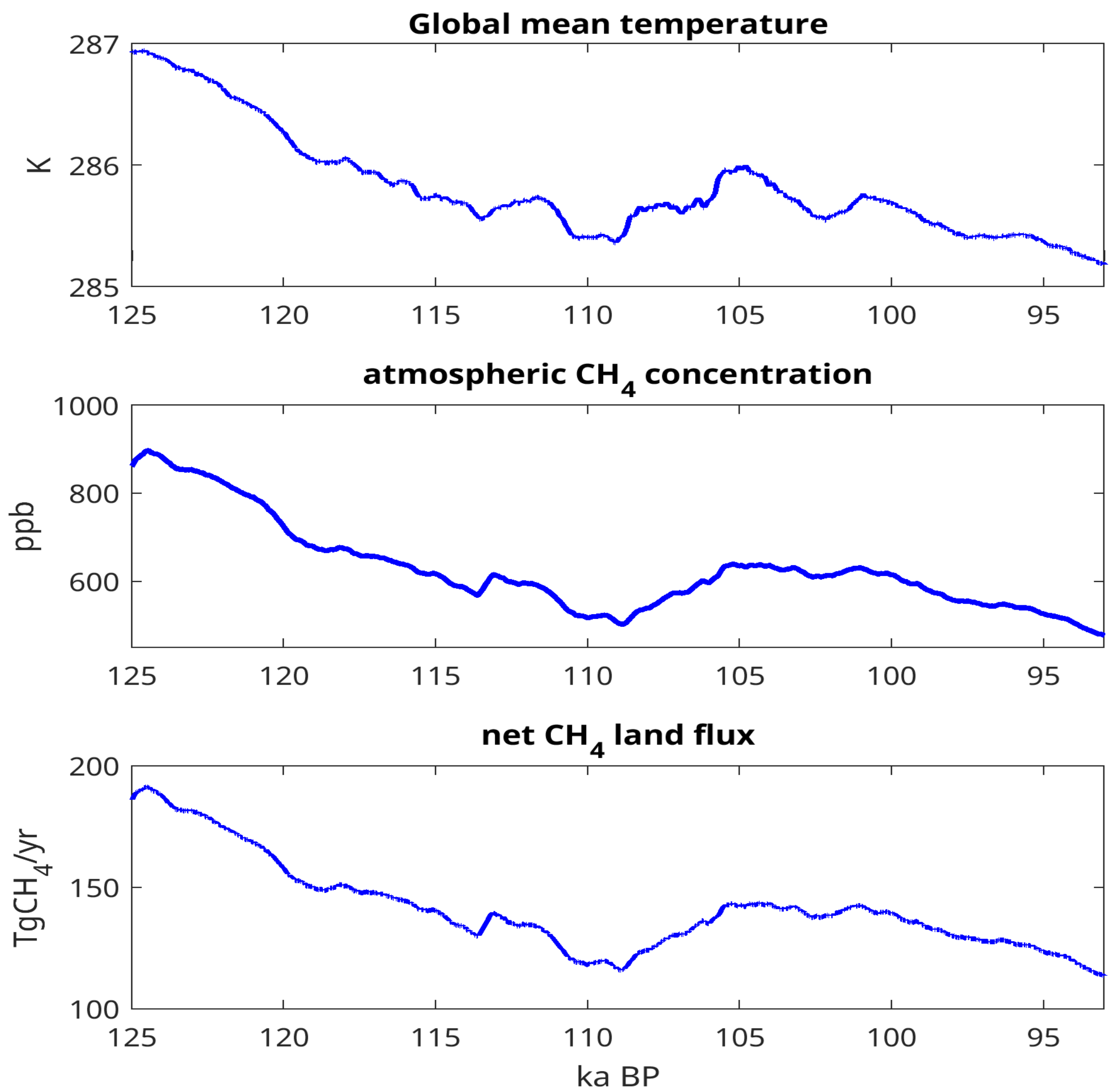

Fig. 2.3-3: Glacial inception in MPI-ESM: Global mean temperature (top), atmospheric CH_4 concentration (centre) and net land CH_4 flux (bottom).

3) WP 2.3 "Methane cycle" (MPI-C)

Within the reported 2021–2022 period we have conducted experiments investigating atmospheric composition variations using the AC-GCM EMAC and the instructive Monte-Carlo based box-model (MCBM). The analysis of the simulation results focussed on deglaciation, in particular on the Mid-Holocene period (MH, 6 ka BP). A set of tools were developed for preparation of the boundary conditions for EMAC from the output of the MPI-ESM system, in particular for any period throughout the last deglaciation (simulated in transient experiments by MPI-M within the WP2.3). Most of the Mistral and Levante systems work was used for resource-intensive simulations with EMAC, which is an AC-GCM with a comprehensive multi-phase kinetic chemistry representation (including air O_2 clumped isotope composition), treatment of aerosol/dust interactions and on-line trace-gas emission sub-models, etc.

Multiple sensitivity experiments were simulated for each time slice for further tuning of the CH4 lifetime parameterisation used in the MPI-ESM. The results for MH confirm that the latter is applicable on inter-glacial scales and contribute to final publication on CH_4 lifetime parameterisation (Gromov et al. 2022).

We have further exploited clumped O_2 isotope composition ($^{18}O^{18}O/^{16}O^{16}O$ ratio deviation from the statistically expected distribution, denoted Δ_{36}) to tackle several open research questions regarding the MH atmospheric climate state. EMAC simulations indicate that conventional ESMs have difficulties simulating the observed MH low-Δ_{36} signal (see Fig. WP2.3M1) which, however, appears to coincide with the MH local minimum in CH_4. Such can be attributed to (i) over/under-parameterisation of atmospheric (thermo-)dynamics, (ii) potentially missing kinetic reactions representation and (iii) changes to trace gas emissions ensuing from these. Whilst there is no indication of (ii) until new experimental evidence appears, potential candidates for (i) are the stratosphere-troposphere air exchange (STE), convection-lightning intensity and tropospheric lapse rate variations that are not adequately simulated by ESMs.

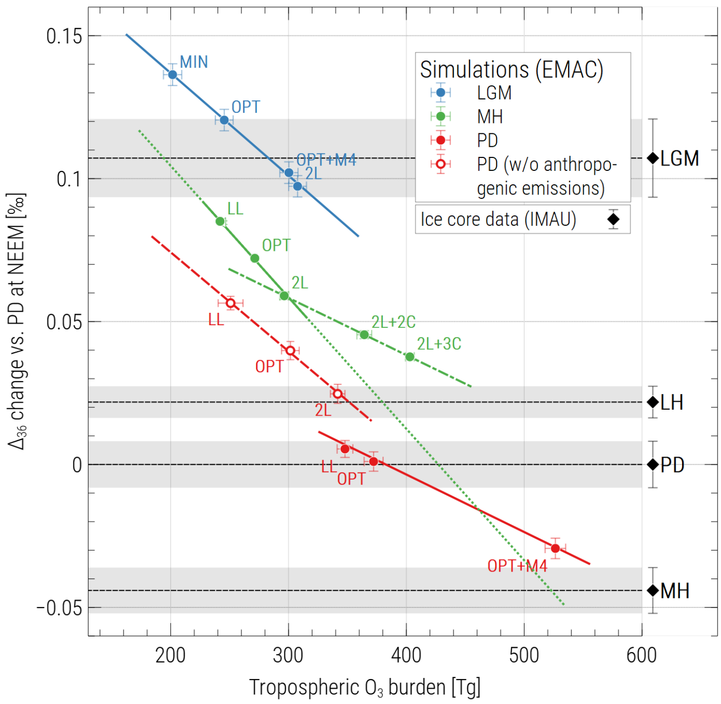

Fig. WP23M1. Δ_{36} values as a function of the total tropospheric O_3 burden for various model calculations representing the Last Glacial Maximum (LGM, blue), Mid Holocene (MH, green) and Present-Day (PD, red) climate and the measurements (black, from Figure 1), all relative to the PD values simulates with EMAC. Different solid symbols indicate calculations with different total amounts of O_3, including sensitivity tests (e.g. OPT: Reference simulation in the given climate state; LL: low lightning NOx; 2L: doubled lightning NOx; 2C and 3C: doubled or tripled organic precursors from surface emissions; M4: quadrupled CH_4 concentrations). Open red symbols show PD simulations without anthropogenic O_3 precursor emissions. Solid and dashed lines are fits through the model results with different O_3 burdens in the different climate states. Black symbols refer to the ice core measurements (including the value *for the Late Holocene, LH). Projections for MH indicate that unrealistically high O_3 burden-only increase is required to reproduce the observed MH Δ_{36} values, hence other mechanisms (STE change, middle-upper troposphere warming, vertical redistribution of O_3) should be involved as well.*

Since EMAC strongly indicates that trace gas emissions/changes in atmospheric chemistry alone cannot explain very low MH Δ_{36} values, we used an instructive MCBM which permits studying STE and tropospheric temperature variations in a more versatile but simplified framework. The MCBM probes for tropospheric and stratospheric end-member Δ_{36} signatures (which vary with air temperature), tropospheric isotope exchange rate (proportional to O_3 burden) and STE for combinations permitting the observed Δ_{36} values changes with respect to present-day (PD) conditions. Fig. WP23M2 demonstrates the results obtained with MCBM (simulated on Levante withing the advanced MC HPC engine) for the MH and LGM conditions for the case when upper-tropospheric and lower stratospheric temperatures experience similar changes. These agree with the EMAC-predicted changes to tropospheric temperatures in LGM (ibid., lower right panel, e.g. 4K colder at about 40% less O_3), however suggest a comparable warming in the MH. The publication on these findings combining results from both models (EMAC and MCBM) are to be submitted in nearest future (Laskar et al. 2022).

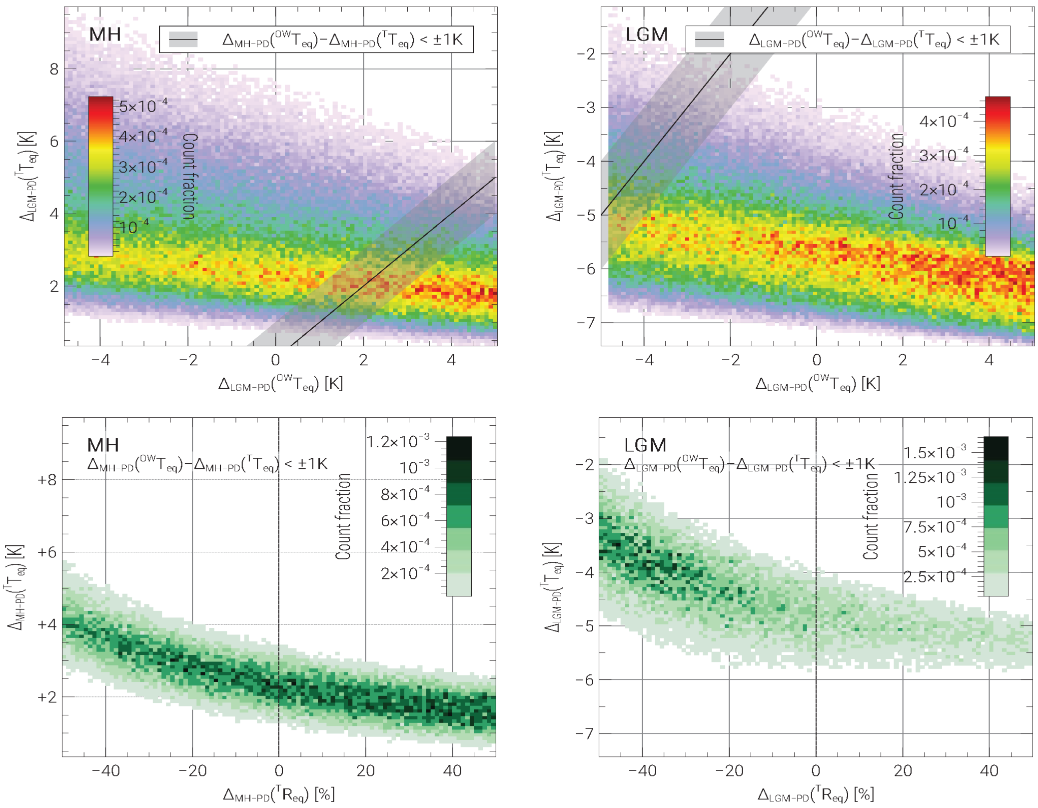

Fig. WP23M2. Results with MCBM simulations of the conceptual tropospheric Δ_{36} model for the Mid Holocene (left) and Last Glacial Maximum (right) periods. Upper panels show the 2D histograms of all possible changes to stratospheric ($^{OW}T_{eq}$) and mid-upper tropospheric ($^{T}T_{eq}$) temperatures of O_2 isotope equilibration permitting the observed Δ_{36} variations w.r.t. present-day (PD) conditions. Lower panels show differences in tropospheric exchange rate (TReq) and tropospheric temperature proxy (vertical axis), also shown relative to the PD values. These differences are required to reproduce the measured signal in Δ_{36}, keeping upper stratosphere-lower troposphere temperature changes similar within 1 K.

Last but not least, output from simulations with MPI-ESM for LGM was used to support novel terrestrial climate proxy evaluations (in-kind contribution). High frequency output for 30 years was derived and processed to obtain past wind regime and precipitation statistics (in comparison to the PD conditions data from reanalyses) for explaining the observed signals in European and Australian terrestrial proxies (see Fitzsimmons and Gromov (2022), Prud'homme, et al. (2022)). For these tasks, we were content to use storage facilities and high parallelism of Levante for performing an unprecedented large set of back-trajectory simulations using MPI-ESM generated climate output.

To recap, we have use about 17% of total allocated (25% of total used) resources in the bm1030 on Mistral in 2022. These numbers are much more modest for Levante (4% and 14%, respectively) because the changeover to the new system occurred at the time when we were mostly done with the resource-intensive simulations with EMAC and performed the analysis of the results (our participation in next PalMod phase is not envisaged). For our modelling systems, the transition to Levante occurred relatively smooth, with an exception of some compilers not working out-of-the box (which DKRZ user support kindly and promptly helped us to solve). We also note sporadic post-processing node failures that lead to incorrect (however repairable) analysis of the model results, which became less frequent recently.

2.2 Publications and references

Publication in 2022

Dallmeyer, A., Kleinen, T., Claussen, M., Weitzel, N., Cao, X., and Herzschuh, U.: *The deglacial forest conundrum*, Nature Communications, in press, 2022.

Kleinen, T., Gromov, S., Steil, B., and Brovkin, B.: *Atmospheric methane since the LGM was driven by wetland sources*, Climate of the Past, submitted.

Liu, B., Six, K. D., and Ilyina, T.: *Incorporating the stable carbon isotope 13C in the ocean biogeochemical component of the Max Planck Institute Earth System Model*, Biogeosciences, 18, 4389–4429, doi:10.5194/bg-18-4389-2021, 2021.

Liu, B., Ilyina, T. and Maerz, J.: *Impact of ocean circulation and marine biological pump on glacial marine biogeochemistry in MPI-ESM*, in preparation.

Fitzsimmons, K. E. and S. S. Gromov (2022). *Northward expansion of the westerlies over glacial southeastern Australia: evidence from semi-arid lunette dunes, temperate basalt plains, and wind modelling*. Front. Earth Sci. 10.

Gromov, S., V. Brovkin, C. Brühl, T. Kleinen, J. Lelieveld and B. Steil (2022). *Atmospheric CH4 lifetime variations on glacial-interglacial timescales*. Clim. Past (in prep.).

Laskar, A. H., G. A. Adnew, S. S. Gromov, R. Peethambaran, B. Steil, J. Lelieveld, T. Blunier and T. Röckmann (2022). *Large variations in atmospheric oxidants and temperature during the Holocene* (in prep.).

Prud'homme, C., P. Fisher, O. Jöris, S. Gromov, M. Vinnepand, C. Hatté, H. Vonhof, O. Moine, A. Vött and K. Fitzsimmons (2022). *Millennial-scale Land-surface Temperature and Soil Moisture Reconstruction Derived From Last Glacial European Loess Sequences*. Nat. Comm. (accepted).

References

Maerz, J., Six, K. D., Stemmler, I., Ahmerkamp, S., & Ilyina, T.: *Microstructure and composition of marine aggregates as co-determinants for vertical particulate organic carbon transfer in the global ocean*. Biogeosciences, 1–55. http://doi.org/10.5194/bg-2019-378, 2019.

Kleinen, T. *et al.*: *Terrestrial methane emissions from the Last Glacial Maximum to the preindustrial period*. *Climate of the Past*, 16(2):575–595, 2020.

Lambert, F. *et al.*: *Centennial mineral dust variability in high-resolution ice core data from Dome C, Antarctica*, Clim Past, 8, 609−623, doi: 10.5194/cp-8-609-2012, 2012.

Peterson, C. D., L. E. Lisiecki, and J. V. Stern: *Deglacial whole-ocean δ13C change estimated from 480 benthic foraminiferal records*, Paleoceanography, 29, 549–563, doi:10.1002/2013PA002552, 2014.

Voulgarakis, A. *et al.*: *Analysis of present day and future OH and methane lifetime in the ACCMIP simulations*, Atmos. Chem. Phys., 13, 2563−2587, doi: 10.5194/acp-13-2563-2013, 2013.

Wild, O. and Prather, M. J.: *Excitation of the primary tropospheric chemical mode in a global three-dimensional model*, J. Geophys. Res. Atm., 105, 24647−24660, doi: 10.1029/2000JD900399, 2000.

Skinner, L., Primeau, F., Freeman, E. et al. *Radiocarbon constraints on the glacial ocean circulation and its impact on atmospheric CO2*. Nat Commun 8, 16010 (2017). doi: 10.1038/ncomms16010.

Yu, J., Menviel, L., Jin, Z.D. Anderson, R. F., Jian, Z., Piotrowski, A. M., Ma, X., Rohling, E. J., Zhang, F., Marino, G., McManus, J. F. (2020) *Last glacial atmospheric CO2 decline due to widespread Pacific deep-water expansion,* Nat. Geosci. 13, 628–633, doi: 10.1038/s41561-020-0610-5.

Jonkers, L., Cartapanis, O., Langner, M., McKay, N., Mulitza, S., Strack, A. and Kucera, M. (2020). *Integrating paleoclimate time series with rich metadata for uncertainty modeling: strategy and documentation of the PalMod 130k marine paleoclimate data synthesis*. Earth System Science Data, 12 (2). pp. 1053-1081. doi: 10.5194/essd-12-1053-2020.

Langner, M. and Mulitza, S. (2019) Technical note: *PaleoDataView – a software toolbox for the collection, homogenization and visualization of marine proxy data*. Climate of the Past, 15 (6). pp. 2067-2072. doi: 10.5194/cp-15-2067-2019.

Schmittner, A. and Lund, D. C. (2015). *Early deglacial Atlantic overturning decline and its role in atmospheric CO2 rise inferred from carbon isotopes (δ13C*), Clim. Past, 11, 135–152, doi: 10.5194/cp-11-135-2015.

3. Project 1029 / WG3

Project title: PalMod WG3 -Datasynthesis
Project lead: M.Werner (AWI)
Subproject lead: T.Läpple (AWI), A.Paul (MARUM)
Allocation period: 01.01.2022 – 30.09.2022

3.1 Report on resources used in 2022

During the year 2022, we have consumed about 50,000 node hours within the framework of PALMOD. The granted numerical resources for our sub-project WP3.3-TP2 were used for a number of simulations including (1) equilibrium simulations under pre-industrial (PI), mid-Holocene (MH), early-Holocene (EH), last interglacial (LIG), and last glacial maximum (LGM), (2) accelerated transient simulations spanning the time periods of 6-0k and 21-9k, as well as (3) a simulation reproducing the cold event around 8.2k with 100-year constant freshwater input over the Labrador Sea. All the above-mentioned experiments were performed using AWI-ESM-wiso, an AWI-ESM model version enhanced by stable water isotope diagnostics.

Due to the late launch of Levante, our simulations were delayed by five months, therefore there are still a significant amount of node hours remaining. The remaining 2022 resources will be used for several stochastic long-term hosing simulations under LGM boundary conditions. The purpose of the experiments is to test the hypothesis that the vast LGM ice sheets of the Northern Hemisphere were in a state of dynamic equilibrium and that the associated stochastic meltwater discharge caused a spatially heterogeneous LGM cooling over the North Atlantic Ocean, which can significantly reduce the discrepancy between modelled and reconstructed LGM sea surface temperature. Such a reduction is a prerequisite for the planned transient simulation of the last deglacial phase. In addition, we will also start a transient simulation starting from our EH experiment covering the last approx. 8,000 years.

3.2 Short summary of achieved results

We took advantage of the most recent release of AWI-ESM with the novel nonlinear free surface formulation, and here we show some results of our simulations.

Pre-industrial

In our report for the previous year (2021) we provided already first analyses of the performance of AWI-ESM-wiso in reproducing the modern isotope distributions in both precipitation and sea water. For further in-depth analyses, we focus primarily on the climate-isotope relationship as simulated by our model and find an overall good performance in simulating observed modern spatial isotope-temperature relationships.

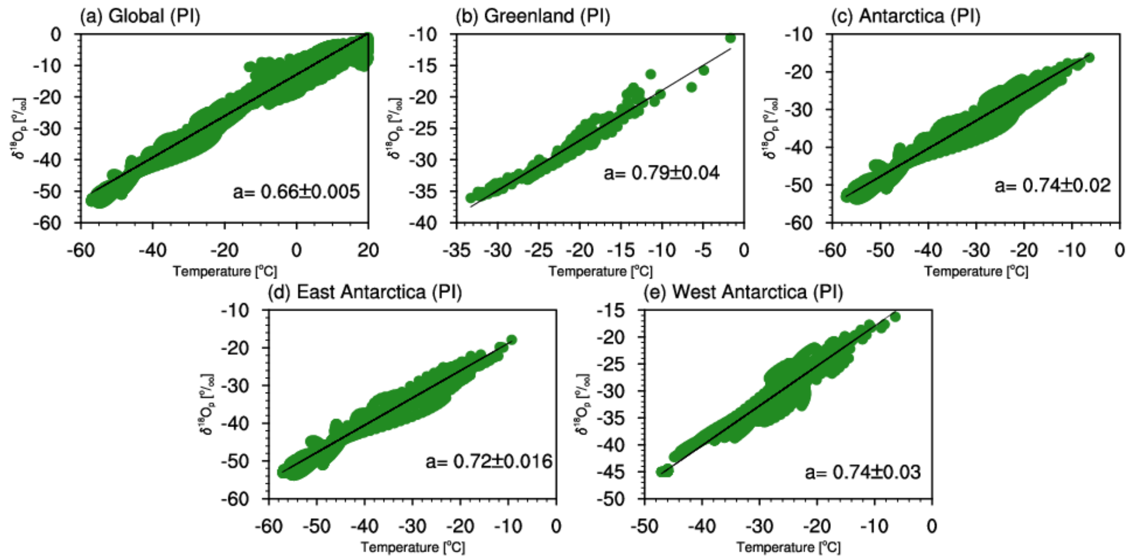

Figure 1. Simulated PI spatial $\delta^{18}O_p$-temperature gradient for (a) all global grid boxes with an annual mean temperature below 20°C, (b) Greenland, (c) Antarctica, (d) East Antarctica, and (e) West Antarctica.

To determine the simulated global spatial $\delta^{18}O_p$-temperature slope, we use the $\delta^{18}O_p$ and surface air temperature modelled at all grid cells with an annual mean temperature below 20°C. This criterion is taken to restrict our analysis to regions with a dominant temperature dependency. Our modelled global spatial $\delta^{18}O_p$-temperature slope has a value of 0.66±0.005 ‰/°C for PI (Fig. 1a), similar to the value of 0.69 ‰/°C derived from observations of the Global Network of Isotopes in Precipitation (GNIP). Compared to former studies using isotope-enabled climate models, our result is better in line with observation. Over Greenland, our modelled $\delta^{18}O_p$-temperature gradients under present-day is both around 0.8 ‰/°C (Fig. 1b), which is somewhat higher than the value obtained from observations (0.67 ‰/°C) and previous model studies using MPI-ESM-wiso (0.71 ‰/°C) and ECHAM4 (0.58 ‰/°C). We are still looking into the reasons for this difference. For Antarctica, our model produces a spatial isotope-temperature slope of 0.74 ‰/°C (Fig. 1c), similar to the mean observed value of 0.8 ‰/°C for modern climate. Moreover, we find no clear distinction of the spatial isotope-temperature relationship between West and East Antarctica. For East Antarctica, our simulated spatial δ18Op-temperature gradient is around 0.73 ‰/°C, and for West Antarctica, the value is fairly comparable at 0.74 ‰/°C, under present-day climate condition (Fig. 1d,e).

Interglacial climate

Figure 2 presents the simulated and reconstructed anomalies in precipitation-weighted annual mean $\delta^{18}O_p$ between PI and the three interglacial time intervals (MH, EH, LIG) under investigation. The climate differences due to changes in insolation and greenhouse gas leave noticeable imprints on the isotope composition of precipitation, with $\delta^{18}O_p$ enriched by up to 1 ‰ in MH with respect to PI. Such change may mainly reflect the regional warming during summer. Another clear picture from Fig. 2 is the depletion of $\delta^{18}O_p$ over North Africa (more than -4 ‰) and South Asia (up to -3 ‰), closely correlated with increased monsoonal rainfall and reduced surface air temperature. The Antarctic continent is generally dominated by enriched $\delta^{18}O_p$ except for parts of East Antarctica that are slightly depleted. Over the remaining land surfaces, AWI-ESM-wiso simulates small to moderate negative MH-PI changes down to -1‰. Concerning the ocean, our model presents more positive $\delta^{18}O_p$ values over the Indo-Pacific warm pool, as a consequence of reduced precipitation during the MH. In addition, large positive $\delta^{18}O_p$ anomalies in the Amundsen Sea are produced by our model because of a pronounced JJA warming in MH relative to PI. Similar results are found in our EH and LIG experiments, but with a more pronounced magnitude. Our model results in terms of MH-PI $\delta^{18}O_p$ changes agree well with speleothem and ice core records for the $\delta^{18}O_p$ changes over Greenland, Eurasia, and East Antarctica. While AWI-ESM-wiso simulates a uniform decrease in $\delta^{18}O_p$ across North and South America, speleothem data reveals a wide range of $\delta^{18}O_p$ changes, being from -1 ‰ to +2 ‰, which may reflect very localized environmental conditions like the cave temperature and atmospheric flow. Moreover, our model captures quite well the signs of the $\delta^{18}O_p$ changes over East Antarctica. Nevertheless, the positive MH-PI isotope changes over West Antarctica simulated by our model are in contrast to several ice core records. For the EH, our model captures well the $\delta^{18}O_p$ changes over Eurasia, Africa and part of South America. However, the negative anomalies indicated by AWI-ESM-wiso are opposite to the proxy records. There are relatively fewer proxy for the LIG period, but both our model and the reconstruction show positive $\delta^{18}O_p$ changes over Greenland and Antarctica.

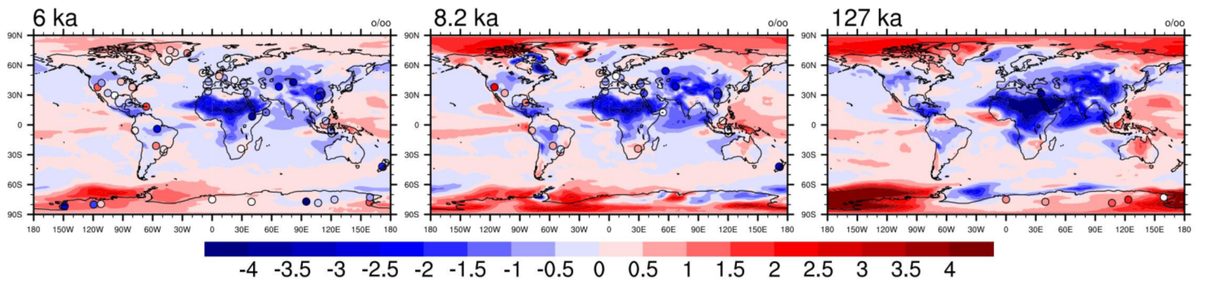

Figure 2. Simulated (shading) and reconstructed (circles) anomalies in precipitation-weighted annual mean $\delta^{18}O_p$ relative to PI in (left) MH, (middle) EH, and (right) LIG. Units: ‰.

LGM

For the simulation of the last glacial maximum, analyses and improvements of our AWIESM-wiso simulations are ongoing. Figure 3 shows a comparison of modeled vs. reconstructed anomalies in annual-mean $\delta^{18}O_p$ (LGM-PI). We find that AWIESM-wiso has a good performance on simulating the glacial change in $\delta^{18}O_p$ in precipitation over locations of the sub-tropical speleothems as well as Antarctic ice cores. The simulated $\delta^{18}O_p$ changes between LGM and PI indicate an overall depletion in $\delta^{18}O_p$ over regions of the LGM ice sheets, consistent with the ice core reconstructions. However, due to a local warming bias simulated in our LGM experiment for the Baffin Bay, the coastal area of north-western Greenland present a pronounced increase in the $\delta^{18}O_p$ values, which largely deviates from the ice core observation showing a glacial isotope depletion of more than -12 ‰. Our analyses indicated that the lack of an ice-berg component with a related isotopically depleted meltwater flux might be responsible for this model bias. Therefore, in a second LGM simulation we prescribed iceberg-related fluxes of freshwater, heat and isotope composition based on outputs from an ice sheet model PISM. This work was done in close cooperation with the physical ice sheet modelling work done in WG1. Fig. 4 clearly illustrates the improvement in the simulated $\delta^{18}O_p$ changes, with the calculated root mean square error (RMSE) reduced from 4.22 to 3.60‰.

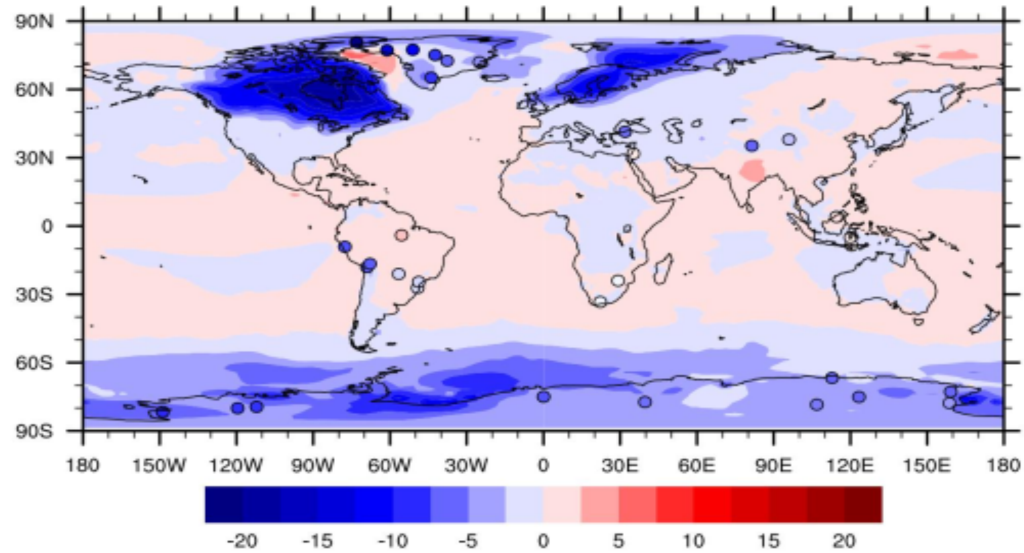

Figure 3. Simulated (shading) and reconstructed (circles) anomalies in precipitation-weighted annual mean $\delta^{18}O_p$ between LGM and PI. Units: ‰.

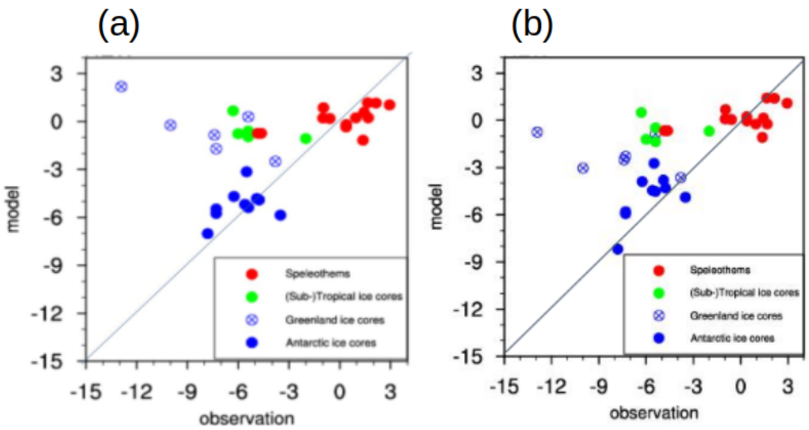

Figure 4. (a) Scatter plot of modelled-versus-reconstructed $\delta^{18}O_p$ anomalies between thee LGM and PI climate. (b) Same as in (a) but for an LGM simulation with prescribed iceberg-meltwater discharge. Units: ‰.

21-0k transient simulation

During the year 2022, We have started the setup and transient simulation of the last deglaciation with AWIESM-wiso. To save computational resources and due to the delayed installation of Levante, we decided to perform a first 21-0k transient simulation with an acceleration technique. The simulations is initialized from the LGM equilibrium run described above. During the integration, orbital parameters, concentration of greenhouse gases as well as ice sheet configurations are updated every model year with values representing deglacial changes that occurred over 100 calendar years. For the ice sheet configuration, we use the GLAC1D reconstruction. The simulated evolution of the North America temperature is shown in Fig. 5, which indicates a gradual warming trend from 21 k to 15 k, followed by a sudden Bølling-Interstadial warming starting at around 14.8 k, which is mainly driven by the retreat of the Laurentide ice sheet. Our model reproduces well the cold event of Younger Dryas. The most recent warm episode simulated in our run happens at mid-Holocene, then the temperature gradually reduces from 6 k to present. As shown in Fig. 5, $\delta^{18}O_p$ changes in precipitation follow in first order the temperature changes, but can clearly deviate on a decadal to centennial time scale. Furthermore, the modelled temporal $\delta^{18}O_p$-temperature gradient over North America does not appear to have remained constant during the simulation period.

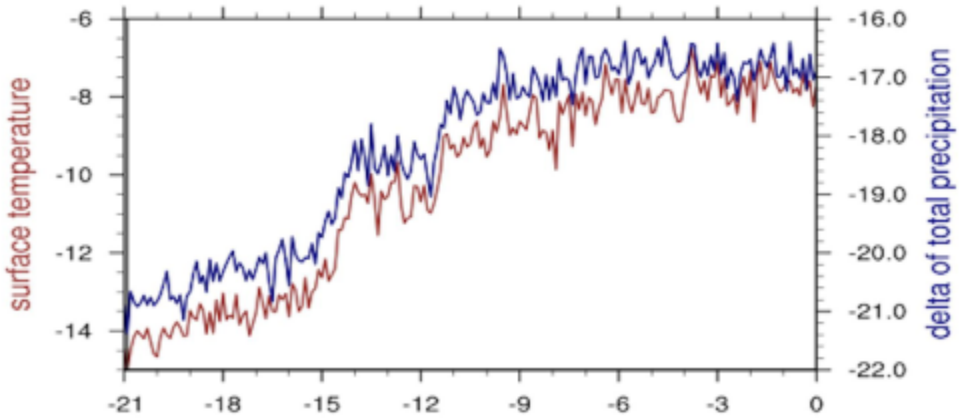

Figure. 5 Time series of temperature (red line, axis to the left, units: °C) and $\delta^{18}O_p$ (blue line, axis to the right, units: ‰) over North America.

Future plan

The remaining resources in 2022 will be used for several long-term stochastic hosing simulations under the LGM boundary conditions as well as a transient simulation starting from 8.2 k. In cooperation with the physical modelling of WG1 we will also continue working on the proposed transient simulations of the last deglaciation and the last inception. For 2023, details of our work plan are described in the computing resources application request.

3.3 Publications

Published

Shi X., Werner M., et al. "Calendar effects on surface air temperature and precipitation based on model-ensemble equilibrium and transient simulations from PMIP4 and PACMEDY." Climate of the Past 18.5 (2022): 1047-1070.

Shi X., Werner M., Wang Q., Yang H., and Lohmann G. "Simulated mid-Holocene and last interglacial climate using two generations of AWI-ESM." Journal of Climate (2022): 1-40.

Under review

Shi X., Werner M., D'Agostino R., Yang H., and Lohmann G. “Why is the Last Glacial Maximum climate so different from today: A model sensitivity study based on AWI-ESM” submitted to EPSL (under review).

Jonkers L., Laepple T., Rillo MC., Dolman AM., Lohmann G., Paul A., Mix A., Shi X., and Kucera M. “Fossil plankton biogeography implies dynamic Last Glacial Maximum ice sheets”, submitted to Nature Geo (under revision).

To be submitted

Shi X., Cauquoin A., Lohmann G., Wang Q., Yang H., Jonkers L., Sun Y., and Werner M. "Simulated stable water isotopes during the mid-Holocene and pre-industrial using AWI-ESM-wiso".

4. Project 993 / CC1

Project title: PalMod CC: Cross-cutting activities
Project lead: H.Bockelmann (DKRZ)
Subproject lead: T.Slawig (Uni Kiel), R. Winkelmann (PIK), K.Rehfeld (Uni Heidelberg), O.Bothe(Hereon), A.Hense(Uni Bonn)
Allocation period: 01.01.2022 – 31.09.2022

4.1 Report on resources used in 2022

Work Package CC.1-SP1– Enabling high throughput for coupled ESMs

As this subproject follows the aim to increase the integration rate of coupled ESMs within PalMod, we used the resources to develop and test several optimisation approaches for the entire model setups used in WG1 and WG2. In particular, we enabled usage of concurrent execution schemes in MPI-ESM and AWI-ESM to increase the parallelism.

AWI-ESM

Since the calculations for individual iceberg trajectories in AWI-ESM can be performed almost independently of each other, a computationally intensive loop was parallelised over all icebergs in addition to the previous asynchronous approach. If a larger number of icebergs need to be calculated, a further speed-up can be achieved, as the following table shows. In this case, the FESOM Iceberg application was started twice, so to speak, and the iterations of the loop over all icebergs were split between the two instances. In combination with the asynchronous method in the sense of a twice parallel approach, the Iceberg calculations should be reduced for optimal overlap so that they do not require more time for the calculation than the other FESOM calculations.

AWI-ESM: ECHAM + FESOM-Iceberg, 40,000 Icebergs					
ECHAM CPU Cores	FESOM CPU Cores	Cluster	Cluster Nodes	Iceberg Calculation	SYPD
256	256	Levante	4	Classical	11.67
256	512	Levante	6	Asynchronous	17.27
256	512	Levante	6	Parallel Loop	15.29
256	1024	Levante	10	Asynchronous + Parallel Loop	23.30

In connection with the investigation of ocean biogeochemistry based on AWI-ESM FESOM-REcoM, an MPI-based approach was implemented to parallelise the computationally intensive tracer loop and thus accelerate the tracer transport calculations. The following table shows for the standalone component FESOM-REcoM which integration rates can be achieved on Mistral or Levante. In terms of hardware, the same number of cluster nodes also results in approximately equal speed increases of about 2.5, as expected. Splitting the loop into 4 FESOM instances also results in approximately equal speedups on both cluster systems. With a combination of both, the model integration rate on Levant is increased by a factor of about 6.5 compared to Mistral.

AWI-ESM: FESOM-REcoM, Standalone, 33 Tracers					
FESOM Instances	**FESOM CPU Cores**	**Cluster**	**Cluster Nodes**	**Tracer Transport**	**SYPD**
1	288	Mistral	8	Classical	8.81
1	1024	Levante	8	Classical	22.88
4	1152	Mistral	32	Parallel Loop (MPI)	22.72
4	4096	Levante	32	Parallel Loop (MPI)	56.73

For fully coupled AWI-ESM FESOM-REcoM, the following table shows how the integration rate can be significantly increased by splitting the tracer transport loop between two FESOM-REcoM instances when the number of nodes is increased from 12 to 20. With a hybrid approach and an alternative implementation of the parallelisation of the tracer loop based on OpenMP, the integration rate of the model can be further improved if the number of nodes is increased from 20 to 36. For the MPI variant of loop parallelisation, very few changes were required in the FESOM source code, which has advantages in terms of readability and maintainability of the source code. This variant is therefore preferred in the PalMod project. Should the reduction of the time to solution be more in focus, the OpenMP variant is available as an alternative and possibly a better compromise.

AWI-ESM: ECHAM + FESOM-REcoM, 33 Tracers						
ECHAM CPU Cores	**FESOM Instances**	**FESOM CPU Cores**	**Cluster**	**Cluster Nodes**	**Tracer Transport**	**SYPD**
512	1	1024	Levante	12	Classical	24.16
512	2	2048	Levante	20	Parallel Loop (MPI)	33.18
512	4	4096	Levante	36	Parallel Loop (OpenMP)	40.22

MPI-ESM

Already in the 2021 allocation period we showed that significant improvements in the throughput rate tend to be accompanied by adjustments in the parallelism in the code (concurrent radiation in ECHAM). This approach was then also applied to the costly calculation of the biogeochemical tracers in the ocean model MPIOM-HAMOCC. As in the above-mentioned consideration of the AWI-ESM FESOM-REcoM model, it is possible here to make the number of resources used directly dependent on the number of tracers used. In this way, the hardware can be optimally utilised and additional computations are taken into account in a scaling manner. The following three figures show how several approaches lead to an overall improvement of 2.8x in comparison to the baseline model on the Mistral system: i/

introduction of concurrency in MPIOM-HAMOCC, ii/ changing hardware to latest generation of CPUs, iii/ combining both steps.

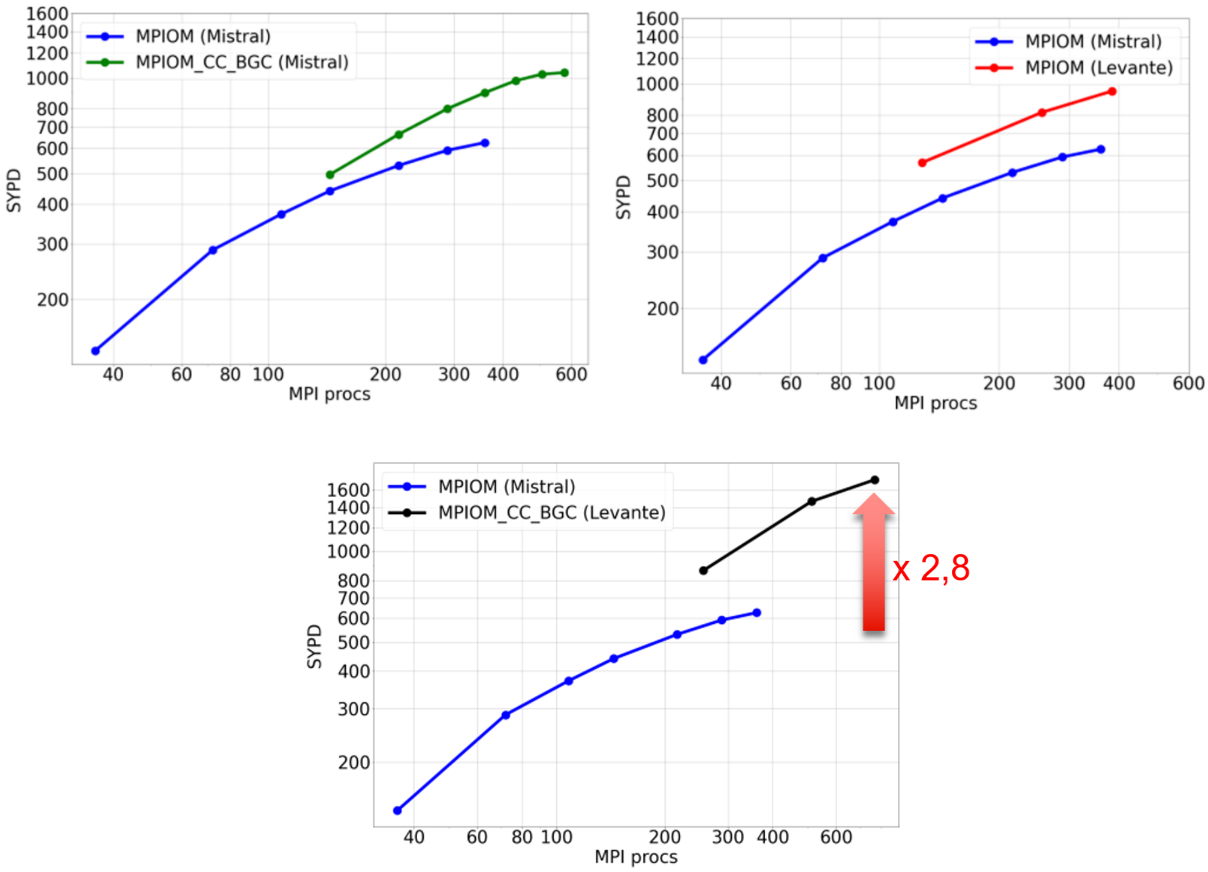

Figure 1: Improvement for model integration rate of MPIOM_HAMOCC based on combined hard- and software approaches.

Finally, in prototypical experiments with the coupled MPI-ESM model, all implemented improvements could be combined:

- Concurrent radiative transfer calculation in ECHAM and concurrent execution of tracer model HAMOCC in MPIOM leading to a runtime improvement of 1.5x
- Utilisation of new AMD EPYC hardware and associated compiler optimisations leading to a minor improvement of 1.3x

Overall, this approaches in summarised in the following scheme and results in a coupled MPI-ESM in T31L31-GR30 being 2.1x faster than the baseline.

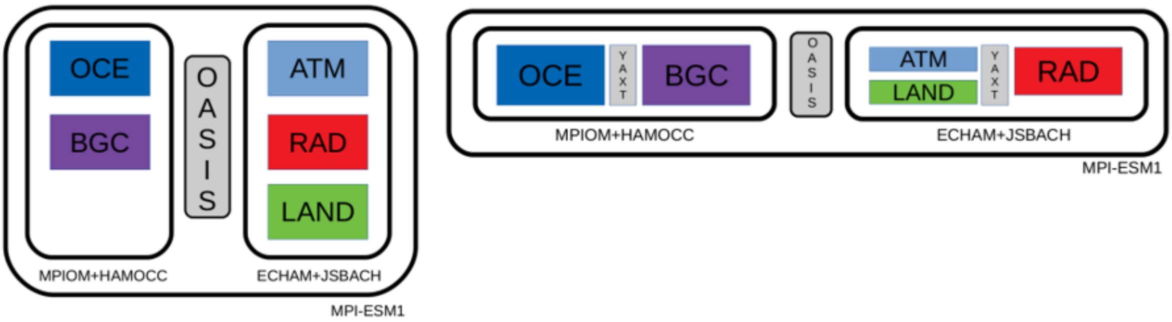

Figure 2: Schematic representation of the concurrent execution of components in the coupled MPI-ESM. On the left before the work in PalMod CC.1, on the right after. The horizontal width represents the number of concurrent parts.

Through this clever combination of improvements in the hardware, but especially through the higher utilisation of the parallelism of concurrent processes, a throughput of well over 1000 SYPD in coarse-resolution could be achieved.

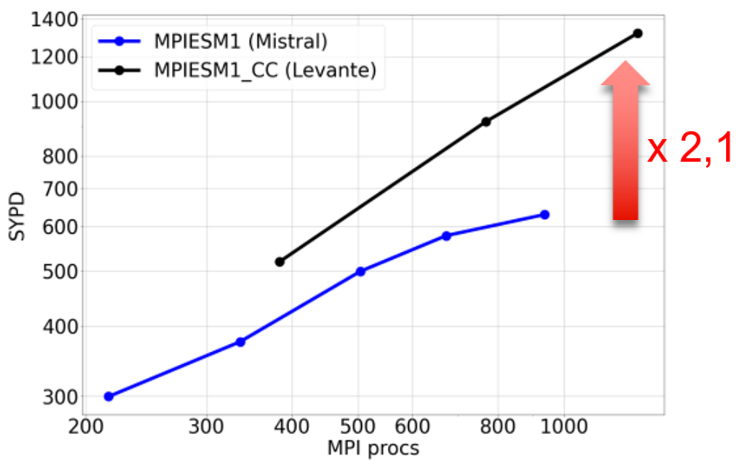

Figure 3: Final improvement for MPI-ESM CR-experiments based on introduction of new hardware and concurrent execution of components.

Work Package CC.1-SP2 – Parallel-in-Time methods for ocean and climate simulations

Two variants of the parareal algorithm for FESOM2 were tested on the HPC systems Mistral and Levante. The first variant corresponded to the classical parareal method for runtime reduction. The basic idea is the approximation of a FESOM2 simulation by an iterative procedure that parallelises the temporal dimension beyond classical domain decomposition. To realise the iteration, the algorithm needs a fast, imprecise procedure and a precise, time-consuming procedure. According to the possibilities of FESOM2, the coarse solver was executed with large time step sizes, the precise solver with smaller time step sizes. To investigate the convergence behaviour, reference solutions were created over different simulation periods and then approximated by the parareal algorithm.

An overview of the experiments and results can be found at https://arxiv.org/abs/2208.07598

For the second variant, the fine and coarse solvers were run on different computational grids, the so-called micro-macro-parareal algorithm. For the coarse grid, the PI mesh was used. For the fine solver, a spatially higher resolution version of the PI mesh was created by a Python tool written for this purpose. To ensure that FESOM2 can simulate with the new grid, various serial test runs with up to 70 years of simulation time were started on Levante. Python tools were then programmed to interpolate between the two meshes and tested on Levante to use the solutions during iteration of the parareal algorithm.

In contrast to the first parareal test series, the aim was to approximate diagnostic variables (e.g. annual mean temperature) and not temporally local simulation results. Since the (diagnostic) simulation results by FESOM2 are significantly dependent on the spatial resolution, a two-level method of parareal iteration was chosen specifically for this purpose. The methodology is described here: https://arxiv.org/abs/1806.04442

The experiments included the approximation of the annual mean temperature over different simulation times (10 years and more). The results on the convergence speed of the micro-macro parareal for FESOM2 are compiled in a paper.

We have found that the efficient use of the non-intrusive algorithm Parareals for complex simulation software such as FESOM2 suffers from the high overhead of data storage and manipulation. Since the results of the fine and coarse simulations have to be stored in files after completion and read in, manipulated and stored again for iteration in Parareal, this procedure generates significant overhead that impairs efficiency and runtime reduction.

Work Package CC.1-SP3– Paleo-lakes in MPI-ESM

A dynamic lake and river model has been developed (for the river model see Riddick et al 2018) and is now fully integrated into the MPI-ESM PalMod transient setup. Progress in 2022 has followed a number of lines:

- Completion of a transient deglaciation run (see fig. 1 for example results) on Mistral using the basic lake and river model after the successful implementation of discharge limiter into the Hydrological Discharge model to prevent glacial outburst floods from crashing the ocean model. This limiter prevents river discharge into the ocean at single point exceeding a threshold; any water exceeding the threshold is stored for later release when the river discharge again falls below the designated threshold.

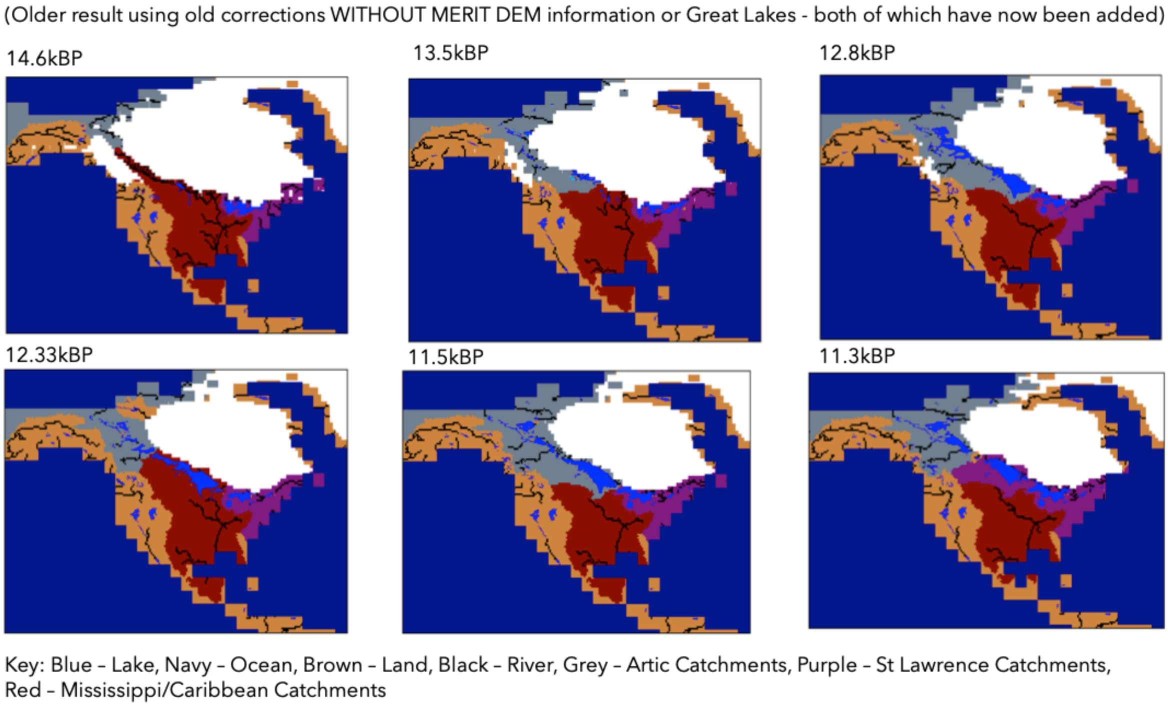

Figure 4: Example result for North America for a coupled run (using a proscribed ice-sheet) of the MPI-ESM PalMod transient model with dynamic lakes and rivers included. This version doesn't use a lake atmosphere coupling (which is still being tested).

- Generation of a new set of present-day corrections by upscaling the MERIT hydro DEM (available from http://hydro.iis.u-tokyo.ac.jp/~yamadai/MERIT_Hydro/) in a hydrological sensitive manner. This was achieved by processing the many individual tiles of the input DEM in groups via SLURM batch jobs on Mistral and then stitching the final result together. The results have been evaluated against the existing current day corrections used by the dynamic river model and have shown improvements in some places. This new set of corrections is also required far fewer manual corrections and will thus produce a more accurate set of dynamic river and lakes for paleo timescales.

- Development and testing of scheme to couple the lake model to the atmosphere. This uses the ideas of the published WEED scheme for wetlands to couple the surface of the lakes to the atmosphere by overloading the existing infrastructure to represent the wet surfaces within vegetation. Considerable effort was required to link this to the lake model on a different grid and timestep and integrate it into the dynamic lake and river setup within the wider MPI-ESM PalMod set-up.

- Infrastructure for careful testing of the overall water budget of the lake model alongside the HD model has been developed and tests of the intra and inter run water balance are ongoing. Early tests have already enabled one significant bug to be removed.

Work Package CC.1-SP3– Land-sea carbon and nutrient transfer in MPI-ESM

In the second part of this subproject and in collaboration with WG2.1 and 2.2, we have updated and adapted a weathering scheme to changing boundary conditions in order to investigate the response of the marine carbon cycle to climate-dependent weathering rates along transient runs of the last deglaciation with the coarse resolution MPI-ESM. Indeed, weathering is a significant process of the carbon cycle at the scale of glacial cycles. It brings out fluxes of carbon, nutrients, and alkalinity to the ocean via rivers. These weathering fluxes have consequences on air-sea exchanges of CO2, but also on the biological pump and carbonate chemistry, which in turn impact the capacity of the ocean to sequestrate carbon. This land-sea process is often not represented (or in a simplistic way) in GCMs, and we are to our knowledge the first group to propose investigating its effects in transient simulations of the last deglaciation.

This adaptation of the weathering scheme builds upon previous developments achieved within the PalMod project. Indeed, transient simulations of the last deglaciation are now run with the global biogeochemical model HAMOCC, taking into account a fully interactive adaptation of the ocean bathymetry, land-sea distribution, and river routing. Ongoing work in WG2.1 now focuses on allowing such simulations to run with prognostic CO2, improved tuning, as well as different ocean physics (e.g. weak/strong background diffusivity leading to a shallow/deep AMOC) in order to assess the impact of the physical state on ocean biogeochemistry. Moreover, an empirical weathering model has been developed in WG2.2. Based on temperature and runoff, different parameterized equations can be used depending on lithology to calculate alkalinity and phosphorus fluxes. Two lithological masks have also been reconstructed for the LGM (21 ka) and present day, taking into account the erosion of loess deposits and the reduction of exposed continental shelves due to sea level rise (Börker et al., 2020). A former version of this empirical model has previously been implemented in HAMOCC as an offline calculation to enable high resolution pre-industrial runs with river inputs (Lacroix et al., 2020). In collaboration with Stefan Hagemann (Hereon), we have largely modified this scheme to allow for the calculation of river inputs for our model resolution from various boundary conditions (land-sea distribution, river routing, ice sheets). Considering the lithologies from Börker et al. (2020), the scheme now uses 10-year temperature and runoff climatologies to compute the alkalinity and phosphorus fluxes released by chemical weathering at a 0.5-degree resolution, integrates these fluxes over each catchment, and finds the ocean grid cell nearest to each river mouth to infer the river inputs of carbon, nutrients and alkalinity.

Preliminary results using the outputs from an already-run transient simulation show that the global phosphorus release increases during the last deglaciation. On the other hand, due to the compensating effects of an increasing runoff and shrinking loess deposits and exposed shelves, alkalinity fluxes display an overall small PI-LGM difference, after larger variations during abrupt events (Fig. 1a). In addition to their climate-dependence, we underline that our river inputs are very heterogeneously-distributed (Fig. 1b), which contrasts with the homogeneous fluxes prescribed at the coast to compensate for the loss to sediment in control runs. This results in biological hotspots at some river mouths, as observed in Lacroix et al. (2020) and in the 500-year PI and LGM time-slice simulations with prescribed CO2 we performed so far. However, we also note that our weathering fluxes are much lower than the default values prescribed to compensate for the loss to sediments (e.g. for alkalinity at the LGM: 0.215 GtC/yr wrt. 0.485 GtC/yr in the control run), which disequilibrate ocean inventories (e.g. drifting whole-ocean alkalinity), underlining the need of an equilibration of sediment fluxes.

This work has led to a poster communication at the International Conference on Paleoceanography (ICP14) and is the subject of a manuscript under preparation. The next steps of this work include: (1) running and equilibrating time-slice runs (with prognostic CO2 and a chosen physical state) with a spin-up(s) using the offline sediment branch; (2) implementing the weathering scheme online (i.e. as a model routine integrated in the set-up of the dynamic topography, land-sea distribution and river routing – that is to say computing river inputs after each 10-year run is completed); (3) running a transient simulation of the last deglaciation with river inputs and comparing it to a control run; (4) running sensitivity tests in time-slice simulations of the LGM to disentangle the effects of the fluxes of carbon, nutrients, and alkalinity and better understand their contribution.

As there are ongoing efforts to implement a similar weathering scheme in CESM (Takasumi Kurahashi-Nakamura), AWI-ESM (Ying Ye), and CLIMBER-X (Matteo Willeit), we also aim to engage an intercomparison study which has the potential to lead to a more robust understanding of the role of weathering.

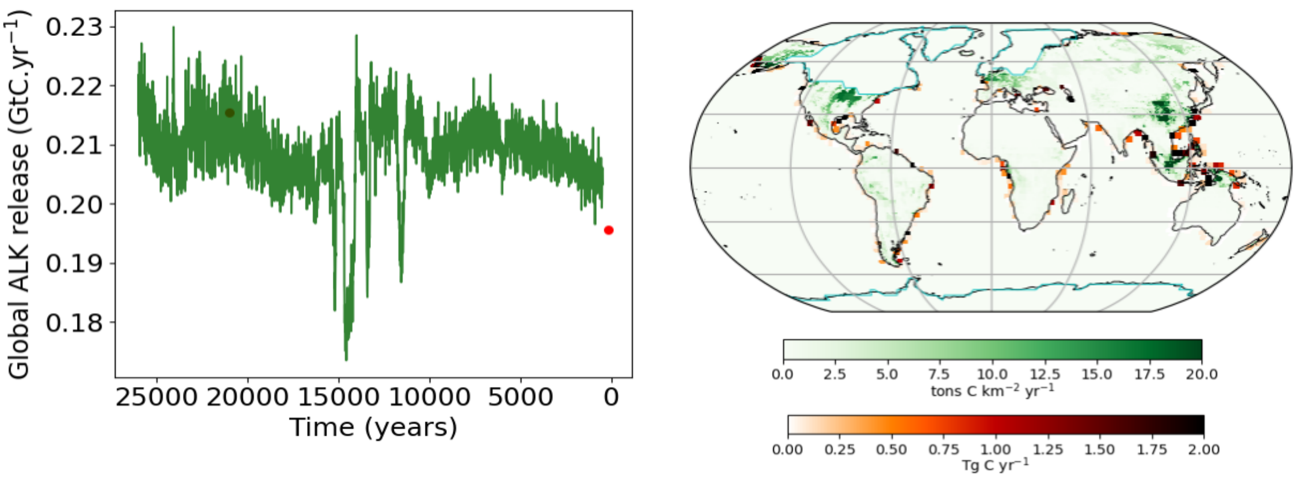

Figure 5: Example result for North America for a coupled run (using a proscribed ice-sheet) of the MPI-ESM PalMod transient model with dynamic lakes and rivers included. This version doesn't use a lake atmosphere coupling (which is still being tested).

Work Package CC.1-SP4 – Development of the PICO ice shelf cavity model into a "pop-up" model for use in transient glacial simulation

There was no explicit request for resources at DKRZ.

Work Package CC.2-SP1-4 – Data management and model data comparison

The data management and model data comparison toolbox development in PalMod have been shifted to project ID bk1192.

4.2 Publications and references

Börker, J., Hartmann, J., Amann, T., Romero-Mujalli, G., Moosdorf, N., and Jenkins, C.: Chemical Weathering of Loess and Its Contribution to Global Alkalinity Fluxes to the Coastal Zone During the Last Glacial Maximum, Mid-Holocene, and Present, Geochem. Geophy. Geosy., 21, e2020GC008922, https://doi.org/10.1029/2020GC008922, 2020.

Extier, T., Six, K.D., Liu, B., Ilyina, T., Paulsen, H.: Local oceanic CO2 outgassing triggered by terrestrial carbon fluxes during deglacial flooding, Clim. Past, 18, 273-292, https://doi.org/10.5194/cp-18-273-2022, 2022.

Lacroix, F., Ilyina, T., and Hartmann, J.: Oceanic CO2 outgassing and biological production hotspots induced by pre-industrial river loads of nutrients and carbon in a global modeling approach, Biogeosciences, 17, 55–88, https://doi.org/10.5194/bg-17-55-2020, 2020.

Riddick, T., Brovkin, V., Hagemann, S. & Mikolajewicz, U., Dynamic hydrological discharge modelling for coupled climate model simulations of the last glacial cycle: the MPI-DynamicHD model version 3.0. Geoscientific Model Development, 11, 4291-4316, doi:10.5194/gmd-11-4291-2018, 2018.

5. Project 1192 / CC2

Project title: PalMod CC2: Datamanagement
Project lead: S.Gehlot (DKRZ)
Subproject lead: K.Peters (DKRZ)
Allocation period: 01.01.2022 – 30.09.2022

5.1 Report on resources used in 2022

To make a large consortia project like PalMod successful, it needs to take care for efficient data exchange between project partners and also with external partners. Therefore, the project bk1192 will be the platform for establishing a framework enabling efficient, timely, and low barrier data exchange. This is necessary because there is an articulated need for improved intra-project collaboration and because storage space on /work is limited.

To ease the communication between the WPs regarding project-internal data needs and data availability, the PalMod Data Management Plan (DMP, PalMod Deliverable D CC.2-1) lists the available and expected data sets and data volumes that will be essential for the future work. The subset of the full PalMod DMP, which is related to the aspects relevant for the DKRZ storage system, builds the core of the DMP supplied with this resource request which can be found in section 7 of the resource application for 2023.

Since the first allocation of space bk1192 in early 2021 (105TB available each for /work and /arch), the PalMod data pool continues to build up and grow in storage with the shared data from project partners (currently using ~178TB, with more data planned to be shared in end 2022). The table below lists the current overview of storage of shared data at bk1192.

Overview storage space for the data project bk1192

Working Group/ Work package	***Lusture work [GByte]***	***HSM arch [GByte]***	***HSM docu [GByte]***
WG 1/ WP 1.1 (MPI-ESM)	***38.608***	***0***	***0***
WG 1/ WP 1.4 (VILMA)	***68***	***0***	***0***
WG 2/ WP 2.1 (MPI-ESM)	***9.100***	***0***	***0***
WG 2 /WP 2.3 (MPI-ESM)	***6.100***	***0***	***0***
WG 3/ WG 3.2	***0.04***	***0***	***0***
WG 1/ WP 1.1 (MPI-ESM) - v2	***112.000***	***0***	***0***
WG 1/ WP 1.2 (AWI-ESM)	***9.884***		
CMORized data storage (temp.)	***700***		
Total used	***178.000***	***0***	***0***

Since August 2021, the PalMod data pool is used as a primary resource for development of model specific CMORization, ESGF publication and WDCC archiving workflows within PalMod-II. Currently the test setups consist of data from all the three coupled PalMod ESMs.

The first set of PalMod experiments for MPI-ESM were published on DKRZ ESGF portal (https://esgf-data.dkrz.de/search/palmod/) in February 2022. The final set of CMORized data is stored at dedicated long term PalMod tape resource (kd1292), along with a backup on bk1192 tape resources. The transient simulations in Kapsch et al., 2022, (https://doi.org/10.1029/2021GL096767), showed, that the ice-sheet boundary conditions, the method of meltwater distribution as well as the model tuning determine the millennial scale climate variability throughout the last deglaciation (Figure 2). To understand these differences is specifically important for the interpretation of multi-model comparisons, e.g. the Paleo Modeling Intercomparison Project Phase 4 (PMIP4) of the last deglaciation, where individual modelling groups can choose between different methods and boundary conditions from a common protocol.

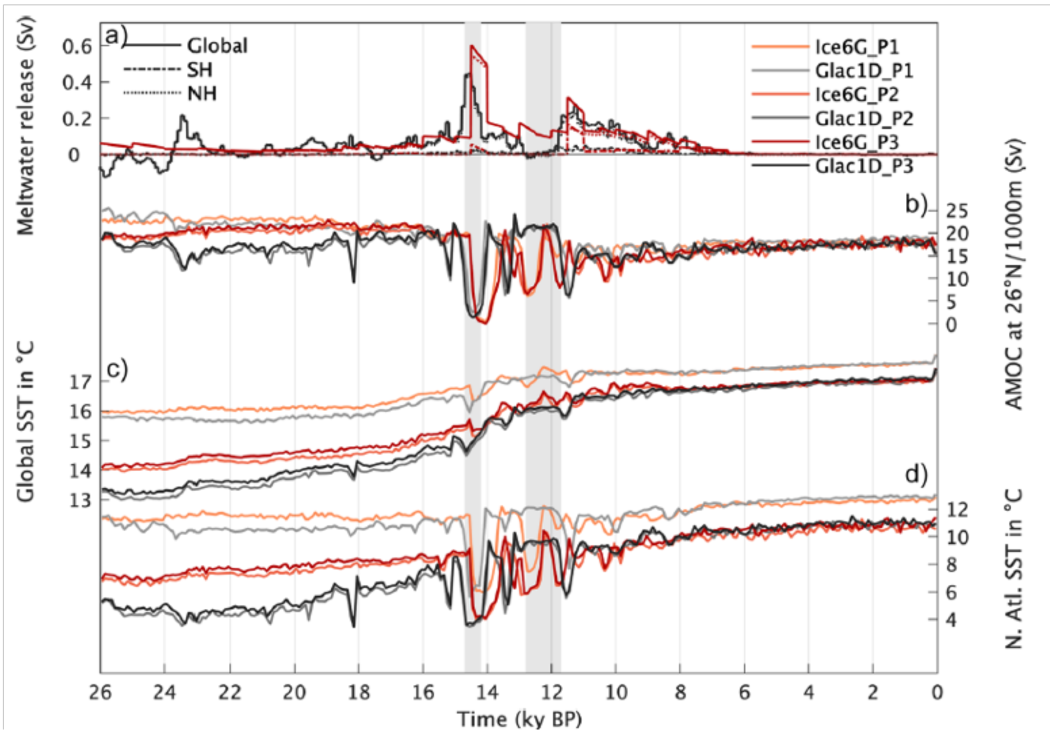

Figure 2: Transient simulations throughout the last deglaciation (Kapsch et al, 2022)